2014

An Experimental Investigation on the Micro Air Vehicle

Shih kang Huang
Wright State University

Repository Citation

Huang, Shih kang, "An Experimental Investigation on the Micro Air Vehicle" (2014). *Browse all Theses and Dissertations*. 1364.
https://corescholar.libraries.wright.edu/etd_all/1364

An Experimental Investigation on the Micro Air Vehicle

A thesis submitted in partial fulfillment
of the requirements for the degree of
Master of Science in Engineering

By

Shih Kang Huang
B.S., Wright State University, 2011

2014
Wright State University

WRIGHT STATE UNIVERSITY

GRADUATE SCHOOL

May 2,2013

I HEREBY RECOMMEND THAT THE THESIS PREPARED UNDER MY SUPERVISION BY Shih Kang Huang ENTITLED An Experimental Investigation on Micro Air Vehicle BE ACCEPTED IN PARTIAL FULFILLMENT OF THE REQUIREMENTS FOR THE DEGREE OF Master of Science in Engineering.

Zifeng Yang, Ph.D.
Thesis Director

George Huang, Ph.D., Chair
Department of Mechanical and Materials Engineering College
of Engineering and Computer Science

Committee on

Final Examination

Zifeng Yang, Ph.D.

George Huang, Ph.D.

Joseph Shang, Ph.D.

Robert E. W. Fyffe, Ph.D.

Vice President for Research and Dean of
the Graduate School

ABSTRACT

Shih Kang Huang. M.S. Department of Mechanical & Materials Engineering, Wright State University. 2014. An Experimental Investigation on the Micro Air Vehicle.

An experimental investigation was conducted to study the flow characteristics of the flow around the flapping wings of a four-wing flapper as well as the lift and thrust coefficient of a four-wing flapper. In the present study, a clap-and-fling type of four-wing flapper was designed and manufactured by using several flexible materials, such as PET film, latex, and aluminized Mylar. Different cross-strut patterns and dimensions of wings were manufactured and tested to optimize the wing designs. In addition to taking the lift and thrust measurements using a highly sensitive force moment sensor unit, a high-resolution Particle Image Velocimetry (PIV) system was employed to achieve detailed flow field measurements to quantify the evolution of the unsteady vortex flow structure around the wings and in the downstream of the flapper. The force measurements were analyzed in correlation with the detailed flow measurements to elucidate the underlying physics to improve our understanding for an optimized flexible wing design and to achieve better performance for flapping wing micro air vehicles. A woofer loudspeaker was employed at the test section where the four-wing flapper was placed to generate sound distances. The effect of different frequencies and amplitudes of sound waves on the aerodynamic performance was investigated. A sensitive force moment sensor unit and PIV system were utilized to measure the lift and thrust and to

take detailed flow field measurements to quantify the effect of sound waves on the flow and wing deformation. The force measurements were analyzed in correlation with the detailed flow measurements and qualitative wing deformation data to elucidate underlying the physics in to improve our understanding of the effect of acoustic disturbances on flexible wings and the overall aerodynamic performance of MAVs.

Table of Contents

LIST OF FIGURES

ACKNOWLEDGEMENTS

I would like to express my deep gratitude to Professor Zifeng Yang, Professor George Huang, and Professor Joseph Shang for their patient guidance and enthusiastic encouragement of this research work. I would also like to thank Dr. Philip Beran and Dr. Richard Roberts for their help on the Vicon system and DIC Data. My grateful thanks are also extended to Mr. Todd Smith, Mr. Jaderic Dawson, and Mr. Jason Chuang, who helped me on the MAV modeling and assembly.

I would also like to extend my thanks to the Lab Manager Greg Wilt and the MME department for their help in offering me the resources to run the program.

Finally I wish to wish to thank my parents for their support and encouragement throughout my study.

1. Introduction

Natural disaster responders, soldiers, and SWAT teams are examples of people who operate in dangerous and potentially hostile environments. Information about their surroundings is desperately needed; having an image/video that provides such information can become a matter of life and death. With the new manufacture and remote control technology, using Unmanned Aerial Vehicles (UAVs) such as the MQ-9 Reaper to support such personnel has become common place. The success of research on UAVs leads scientists to Flapping Wings Micro Air Vehicles (MAVs). Flapping Wings have been widely found in nature for flying birds and insects. Especially small birds and insects exploit the coupling between flexible wings and aerodynamic forces such that the aeroelastic wing deformations improve aerodynamic performance (Mueller, 2001). They use multiple unsteady aerodynamic mechanisms for lift and thrust enhancement and they combine sensing, control, and wing maneuvering to maintain not only lift but also flight stability (Shyy et al., 2010). It has been found that insects, birds, and bats can produce complex motions that can consist of flexing, twisting, bending, rotating or feathering their wings throughout the entire flapping cycle in order to adapt to the varying ambient conditions. However, it is very difficult to accomplish an outstanding maneuverability practically as a bird or insect does. Many studies both from the biologists' side (Rayner, 1979; Lighthill, 1990; Spedding, 1992) and the aerospace engineering side (Maxwothy, 1979; Shyy, 1997; Wang, 2000; Koehler et al., 2012) have been conducted to decode the complicated behavior of insects in their flapping motions. For the successful design of flapping wing vehicles, it will be important to determine which movements of insects and birds are truly necessary for MAVs. In fact, the successful design of MAVs with comparable maneuverability to an insect has become a big challenge. A development of flapping wing micro vehicles including design, CFD, experiment and actual flight testing was given in the recent paper by Hsu et al. (2010). Compared with other designs of Micro Air Vehicles (MAVs), the flapping wing MAV has its unique advantages: 1. distinguished maneuverability such as hovering and quick turns; 2. efficient use of power for propulsion by flapping wings at low Reynolds numbers; 3. low noise generation. Even though helicopter-like MAVs, to some extent, can provide good agility and vertical-take-off-and landing capability, they are too noisy to go undetected while operating reconnaissance missions and usually inefficient for low Reynolds number flight. These advantages make the flapping wing MAV perfect for executing the intelligence, surveillance, and reconnaissance missions in urban, indoor, or battlefield environments. However, we are short of validated theoretical and computational tools to design successful flapping wings. Our knowledge and understanding of the fundamental aerodynamics of flexible wings are still inadequate. To gain detailed temporal and spatial resolved flow field information in an experiment, the advanced flow diagnostic technique, Particle Image Velocimetry (PIV), might be the best tool to be employed to conduct the study.

A number of studies have been carried out in recent years to examine key parameters for the optimization design of a flexible wing. An important factor influencing the thrust generated by a flapping wing is the wing's flexibility. Heathcote et al. (2008) found that span-wise flexibility will affect the thrust: a wing that is either too inflexible or too flexible along the span will not produce as much thrust as a wing with optimum flexibility. Altering the chord-wise flexibility will also affect thrust. Mazaheri & Ebrahimi (2010) found that wings with greater chord-wise flexibility produced 20% less thrust than other wings they examined. In their study, the wings were of identical size, membrane and strut pattern; the researchers increased/decreased the diameter of the cross-struts in order to vary the chordwise flexibility of the wing. Kim, et al. (2008) employed a "smart flapping wing" with a macro-fiber composite actuator to change the camber and chordwise flexibility of a wing. It was found that increasing chord flexibility can reduce the angle of attack versus that of a wing with a rigid chord. This could reduce the size of the leading edge vortex and thus produce additional aerodynamic forces in dynamic test conditions. Le, et al., used a computational model and examined the behavior of a flapping wing under different conditions of chord flexure. As chord flexure amplitude increases, the phase angle of the wing becomes more important. Peak propulsive efficiency occurs at moderate chord flexure amplitude; the greatest amplitude is less efficient than low amplitude.

The thrust produced by a flapping wing is also affected by "skeletal reinforcement," which was named by Pin Wu *et al*. (2010). They showed that wings of identical size and membrane material, flapping at identical frequencies, would produce different thrust forces, depending on the cross-strut placement employed for the different wings. Another study on the effects of wing compliance was performed where researchers designed two wings of identical size and membrane. One wing was designated as "rigid" and had a leading edge spar of greater diameter and additional cross-struts compared to the "more compliant" wing. The "more compliant" wing generated higher thrust and less lift than the "rigid" wing (Mueller et al., 2010). Lift is augmented by increased membrane flexibility for otherwise identical flapping wings during unsteady-state flight. A potential disadvantage of flapping wings is that they have reduced lift and thrust when the forward velocity is relatively large (Hu et al., 2010).

There is additional research that supports the argument that simply increasing wing size will **not** necessarily result in increased thrust. Lin et al. (2006) examined two different types of membrane wings. The largest wing had the greatest span-wise flexibility due to the placement of the cross-struts on the wing. However, the smaller wing that had less span-wise flexibility was found to generate more thrust compared to the larger, more flexible wing when both wings were flapped at the same frequency. Another study on the effect of length was performed in which the membrane of the flapping wing was removed in order to ignore the aerodynamic force produced by the membrane. The researchers increased the length of the reinforcing diagonal “vein” but kept the chord dimension constant. They found that as wing length increases, flapping frequency decreases for a given input voltage (Peng et al., 2009).

There are few studies of flow around flapping wings. Heathcote et al. (2008) employed PIV but conducted the experimental study using a water tunnel, which would affect the inertial effect considerably. Watman & Furukawa (2008) conducted a flow visualization experiment in a wind tunnel but did not perform a quantitative measurement on the flow. The Wright State University Center for Micro Air Vehicle Studies successfully developed a novel model of MAV that used a more powerful motor and had greater mass than the original prototype. However, no emphasis was placed on updating the wing from the original prototype in order to optimize the wing for the new prototype. In the present study, an experimental study was conducted to quantify the effects of flexibility, dimensions, and cross-strut pattern of the wing on the force generation (lift and thrust) as well as the detail of the flow feature around flapping wings. A high-resolution Particle Image Velocimetry (PIV) system was employed to achieve detailed flow field measurements to quantify the evolution of the unsteady vortex flow structure around wings and in the downstream of the flapper. The force measurements were analyzed in correlation with the detailed flow measurements to elucidate underlying physics in order to improve our understanding for an optimized flexible wing design and better performance of flapping-wing micro air vehicles.

The primary missions of MAVs include surveillance missions, detection, and communications. MAVs are expected to perform tasks such as infrared images of battlefield (referred to as the “over the hill” problem) and urban areas (referred to as “around the corner”). These real-time images can give the number and location of opposing forces. This type of information can also be useful in hostage rescue and counter-drug operations (Mueller, 2001). However, there must be a pre-requisite that the MAV is hard to detect and hard to attack in order to make all the above mentioned tasks successful. Compared to other aerial vehicles, the flapping wing MAV has its unique advantages, such as small size, light structures, easiness to disguise as an insect or bird, and low noise emission. However, due to the small size, light structures, and membrane-like wings, any disturbances, such as wind gusts oracoustic disturbances, could produce a fatal impact on the MAV flapping flight.

Many researchers have noted the importance of aeroelastic coupling between the wing and the surrounding fluid and its relation to lift and thrust generation. On the one hand, the wing deformation depends upon many physical quantities such as chord and span length, camber, and especially the mass and stiffness distribution of the wing. On the other hand, dynamic quantities such as the time dependent pressure loading, wing speed, freestream velocity, and local acceleration of the wing surface also directly drive the instantaneous wing deformation (Ho et al.,2003). In addition, disturbances in the flow such as wind gusts and sound disturbances can also drive the wing deformation. Definitely, any changes in the wing deformation will have an impact on the resultant aerodynamic forces. Not only the deformation of wings but also the coupling process can be affected by sound excitations. The techniques of active sound control, known as anti-sound, have been successfully adopted in the control of airfoil flutter (Huang, 1987; Lu and Huang, 1992). Ffowcs Williams (1984) has emphasized the principle that any unsteady linear field that can be monitored, processed, and simulated by a secondary unsteady field is amenable to active control and modification. Nissim (1971) described the general energy principle for flutter suppression that for all stable oscillatory motions of an elastic system in an airstream positive, work must be done by the system on the surrounding medium. Inversely, if positive work is done by the surrounding medium on the system, devastating flutter would happen. Whether a positive work or negative work would be done to the flapping wings is determined by the sound excitations.

Biologists have conducted experimental studies on the response behavior of free flying Lepidoptera in the presence of artificial sound. Some specimens showed inhibitory reactions such as the interruption or cessation of movement, sometimes with complete tonic immobility (Treat, 1955; Baker and Carde, 1978). These phenomena have been entirely attributed to the changes in the physiological condition of their experimental insects. But from an aerodynamicist's point of view, these phenomena might be partly attributed to the sound-induced vibration of the wings or the effect of sound on the coupling between flapping wings and the ambient flow. The insect might fail to adapt to the artificial sound induced vibration of their flexible wings; therefore, the inhibitory reactions were observed.

It will be interesting to see how disturbances affect the flapping flight of an MAV. A great deal of research has been done on the effect of gust (Zarovy et al., 2010, Jones and Yamleev, 2012), but very little attention has been paid to the acoustic disturbances. In reality, it is extremely possible that the MAV might be exposed to an acoustic field, such as noise in a suburban area, sound waves due to artillery fire in the battlefield, or pure artificial sound disturbances from the opposite force. When a sound wave is incident, it induces the membranes to vibrate, and the induced vibration would either enhance or harm the coupling of the complex oscillatory flows and wing deformations. Either the enhancement or harm on the coupling between fluid and flexible wings would significantly change the mechanism that accounts for the generation of aerodynamic force. On the other hand, the sound disturbances could force the flow to transit to turbulent by inducing Tollmien-Schlichting waves (Ricci et al., 2007). Intensive studies have been conducted on the effects of acoustic disturbances on low Reynolds number airfoil flows. Many investigators have noted that the acoustic energy can affect the measured lift and drag on an airfoil (Ahuja et al. 1983; Ricci et al., 2007). Sound at a preferential frequency can postpone the turbulent separation on an airfoil and tend to force the separated flow to reattach to the surface (Yarusevych et al., 2007; Zaman et al., 1991; Suzuki and Ishii, 2000; Hakan et al., 2012). However, to the authors' knowledge, there is no investigation on the effects of acoustic disturbances on the flow over flexible flapping wings. There is a definite need to study the effect of sound disturbances on the aerodynamic performance of MAVs. For example, the sound source can be used to induce flutter of the flapping wings in developing technologies to defend MAV reconnaissance; on the other hand, we can take advantage of the study in developing a dynamic control strategy to help the MAV survive under artificial acoustic disturbances from opposite forces.

In the present study, an experimental study was conducted to qualify and quantify the effects of acoustic disturbances on the wing deformation, the force generation (lift and thrust), as well as the details of the ambient flow feature around flapping wings. A wafer loudspeaker was employed to generate sound disturbances at the test section where the four-wing flapper was placed. The effect of different frequency (20Hz ~ 20000Hz) and amplitude of the sound wave on the aerodynamic performance was investigated. In addition to the lift, thrust, and side force measurements using a highly sensitive force moment sensor unit, a high-resolution digital Particle Image Velocimetry (PIV) system was employed to achieve detailed flow field measurements to quantify the effect of sound waves on flow-structure interactions. The force measurements were analyzed in correlation with the detailed flow measurements and wing deformation data to elucidate underlying physics in order to improve our understanding of the effect of acoustic disturbances on flexible wings and the overall performance of the MAV.

2. Experimental setup

2.1 Four-Wing Flapper Model

A picture of the design of the flapping-wing MAV has been shown in Fig. 1(a). Fig. 1(c) and Fig. 1(d) show the design of the gearing system and dimension of the wing, respectively. The spanwise length (L) of the wing is 190mm; the chordwise width (W) is 80mm. The flexible material used for the flapper is PET film (≈35μm thick). Fig. 1 (b) shows the cross-struts pattern as the skeleton of the wing. The cross-struts were 0.5mm diameter carbon fiber, while the leading edge struts were 0.8mm diameter carbon fiber. The cross-struts were attached to the wing membrane by small pieces of #M Blenderm^{tm} tape; the leading edge struts were attached by 3M Super 77^{tm} spray adhesive.

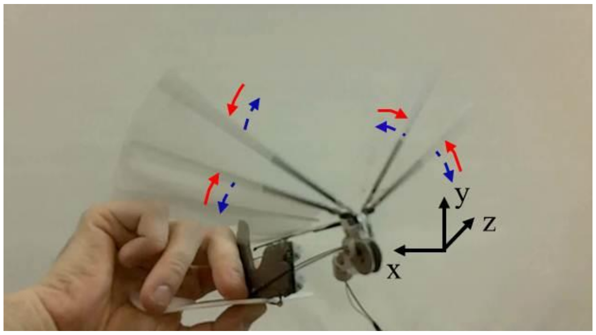

(a). The prototype model of flapping MAV pattern

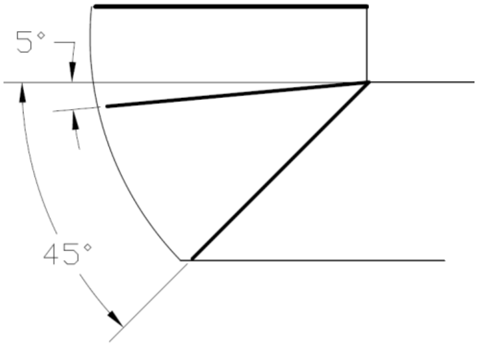

(b). Cross strut

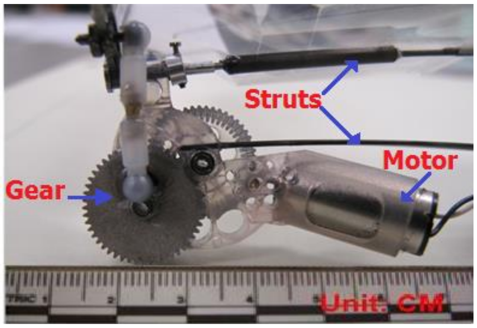

(c). A focus view on the gearing system

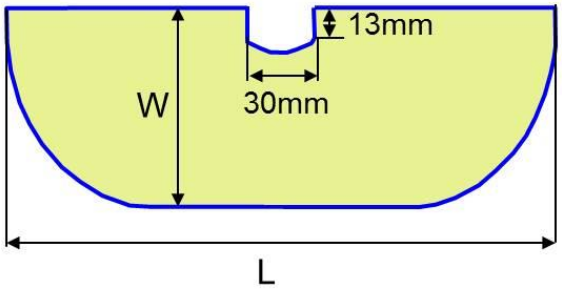

(d). Planer view of the wing

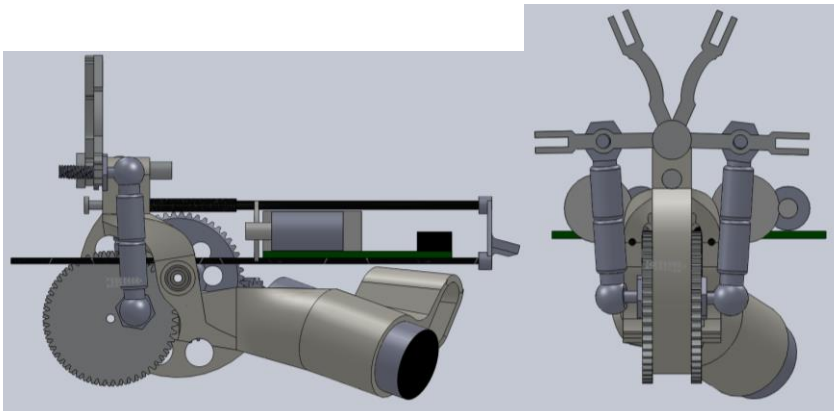

(e)Solid works Side View (f) Solid works Front View

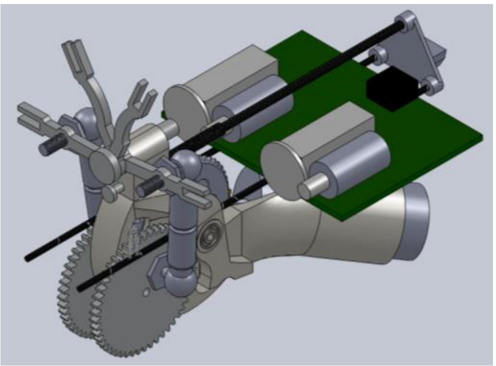

(g) Solid works Isometric View

Figure 1: Four-Wing flapper model

2.2 Low-speed wind tunnel

The experiments were conducted in a low-speed, open-circuit wind tunnel that has a maximum velocity of 40 m/s located in the Department of Mechanical and Materials Engineering at Wright State University. The tunnel has an optically transparent test section of 2 ft × 2 ft (i.e., 610 mm×610 mm) in cross section. The tunnel has a 10:1 contraction section upstream of the test section with honeycombs and screen structures installed ahead of the contraction section to provide uniform, low-turbulence incoming flow into the test section. The turbulence intensity in the center of the test section was found to be about 1.0% of the incoming flow measured by using a hotwire manometer. There is a control box used to control the motor speed and thus the rotation speed of the fan installed at the end of the wind tunnel.

The wind speed was set to 6 m/s and 7 m/s for the present study, which corresponds to 7.71 Hz and 8.77 Hz of the rotation frequency.

2.3. Experimental setup for dynamic wind load and flow field measurements

An ATI Industrial Automation, a Nano-17 load cell was elevated onto a steel shaft in order to minimize ground effects caused by the flapping wings. The steel shaft was attached to an isolation table supported by air cushions. The data acquisition was accomplished by two National Instruments NI 9215 DAQ Cards plugged into an NI DAQ9174 base. The ratio of thrust to weight was calculated by using the expression $R_{TW} = F_x / mg$, where *m* is the weight of the wing. The DAQ cards were provided power by means of an Agilent E3646A Dual Output DC power supply. A Mastech HY3003 DC power supply was used to control the voltage provided to the electric motor actuating the wings. This allowed the team to measure the current draw and power used by the motor. The flapping frequency of the flapping wings was adjusted via control of the voltage and current from the power supply. A Monarch PLT200 laser tachometer was used to measure the frequency of the wing flapping. In the wind tunnel experiment, through a hole on the bottom of wind tunnel, the supporting rod was connected to a high-sensitivity force-moment sensor (JR3, model 30E12A-I40) in order to measure the dynamic aerodynamic force (both force and moment) acting on the four-wing flapper. The JR3 load cell is composed of foil strain gage bridges, which are capable of measuring the forces on three orthogonal axes, and the moment (torque) about each axis. The precision of the force-moment sensor cell for force measurements is ±0.25% of the full range (40N). In the present study, the thrust coefficient (i.e., aerodynamic force coefficients along x –direction) and lift coefficient (i.e., the lift coefficient along y-direction) of the test model were calculated by using the expressions of $C_T = F_x / \frac{1}{2}\rho U_\infty^2 A$, and $C_L = F_y / \frac{1}{2}\rho U_\infty^2 A$ where ρ is the air density and U_∞ is the mean flow velocity. During the experiments, the wind loads data were acquired for 60 seconds at the sample rate of 1,000 Hz for each tested case.

In addition to the wind load measurements, a high-resolution digital Particle Image Velocimetry (PIV) system was also used to achieve detailed flow field measurements to quantify the characteristics of the flow around flapping wings. Fig. 2 shows the schematic of the PIV system used in the present study. For the PIV measurements, the flow was seeded with ~ 1 μm water-based droplets by using a fog generator. Illumination was provided by a double-pulsed Nd:YAG laser (NewWave Gemini 120) adjusted on the second harmonic and emitting two pulses of 120 mJ at the wavelength of 532 nm. The laser beam was shaped to a sheet by a set of mirrors with spherical and cylindrical lenses. The thickness of the laser sheet in the measurement region was about 2 mm. The time interval between the two laser pulses is set to 100 μs . A high resolution 14-bit CCD camera (Pixelfly, CookeCorp) was used for PIV image acquisition with the axis of the camera perpendicular to the laser sheet. The CCD camera and the double-pulsed Nd:YAG lasers were connected to a workstation (host computer) via a Digital Delay Generator (Berkeley Nucleonics, Model 565), which controlled the timing of the laser illumination and the image acquisition. During the experiments, “free-run” PIV measurements were conducted at first in order to determine the ensemble-averaged flow statistics (e.g., mean velocity, turbulence intensity, Reynolds Stress, and turbulence kinetic energy) around and in the downstream of the flapper. It should be noted that the data acquisition rate for the “free-run” PIV measurements was pre-selected at a frequency that is not a harmonic frequency of the rotation frequency of the gears in order to ensure a meaningful determination of the ensemble-averaged flow quantities.

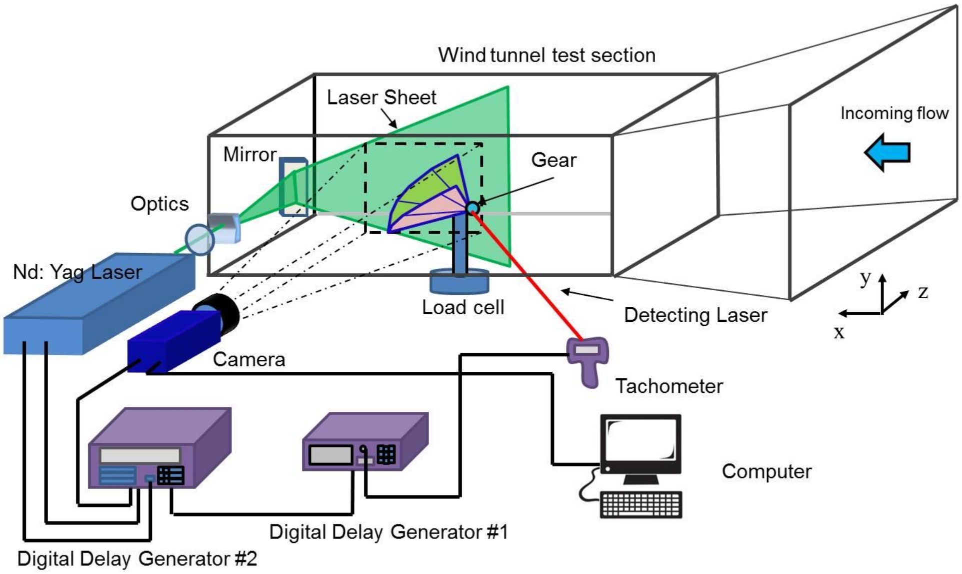

Fig. 2 Schematic of the experimental setup.

Phased-locked PIV measurements were also conducted to elucidate more details about the time evolution of the vortex flows in relation to the position of the flapping wings. In order to achieving the phase-locked PIV measurements, as shown in Fig. 3, a digital tachometer was used to detect the position of a pre-marked gear. The tachometer would generate a pulsed signal as the reflective tape strip on the gear passed through the detecting laser from the tachometer. The pulsed signal was used as the input signal to a Digital Delay Generator (DDG) to trigger the digital PIV system for the phased-locked PIV measurements. By adding different time delays between the input signal from the tachometer and the TTL signal output from the DDG to trigger the digital PIV system, the phased-locked PIV measurements at different phase angles of the flapping wings can be accomplished. At each pre-selected phase angle, 266 frames of the instantaneous PIV measurements were used to calculate the phase-averaged flow velocity distribution in the wake of the wind turbine model.

In the present study, instantaneous PIV velocity vectors were obtained by a frame to frame cross-correlation technique involving successive frames of patterns of particle images in an interrogation window of 32×32 pixels. An effective overlap of 50% of the interrogation windows was employed in PIV image processing. After the instantaneous velocity vectors (u_i, v_i) are determined, the vorticity (ω_z) can be derived. The distributions of the ensemble-averaged flow quantities such as the mean velocity, turbulence intensity, Reynolds Stress, and turbulence kinetic energy were obtained from a cinema sequence of about 1000 frames of the instantaneous PIV measurements. The measurement uncertainty level for the velocity vectors is estimated to be within 2% and 5% for the turbulent velocity fluctuations, Reynolds stress, and turbulent kinetic energy calculations.

3. Wing Improvement

3.1 Experimental Measurement Setup

Four parameters of the wing were identified for experimental examination. These are length, width, materials and cross-strut placement. The increases in length and width are self-explanatory. Three materials were evaluated:

Polyethylene terephthalate (PET) film (≈35μm thick - original wing material), latex (≈152μm thick), and aluminized Mylar (≈20μm thick). The cross-struts were 0.5mm carbon fiber rods oriented diagonally along the span of the wing. In order to systematically change either the span-wise or chord-wise flexibility, three different cross-strut patterns were utilized, as shown in Fig. 3. The first pattern, the default pattern found in the original wing, was to set the strut at 45^{o} to the leading edge. The other two patterns were selected so that one pattern was chordwise flexibility limiting (30^{o} to leading edge) while the other pattern was spanwise flexibility limiting (5^{o} to leading edge). The cross-struts were 0.5 mm diameter carbon fiber, while the leading edge struts were 0.8 mm diameter carbon fiber. The cross-struts were attached to the wing membrane by small pieces of #M Blenderm^{tm} tape; the leading edge struts were attached by 3M Super 77^{tm} spray adhesive. In order to change the size of the wing, the length was set at 100%, 150%, or 200% of the original design; *i.e.*, 190 mm, 270 mm, or 350mm. The width was set at 100%, 110% or 120%, *i.e.*, 72 mm, 80 mm, or 87mm. Fig. 4 shows the basic dimensions of the wing.

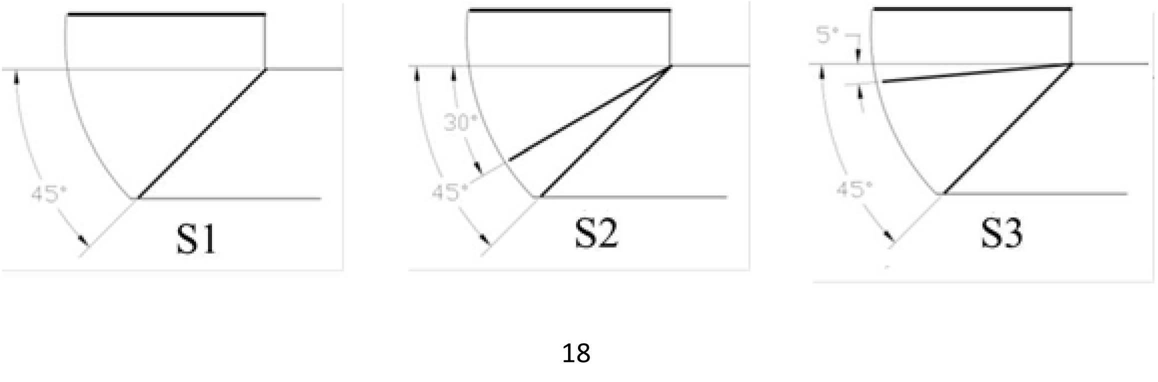

Fig. 3 Three different cross-strut patterns

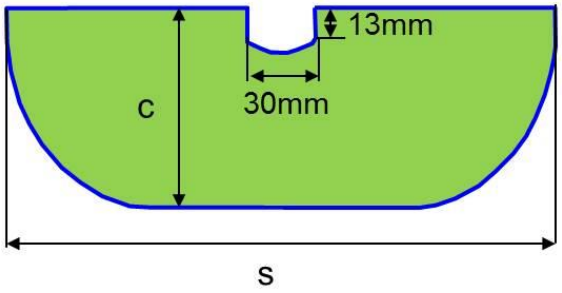

Fig. 4 basic dimensions of the wing

3.2 Result and Discussion

As aforementioned, a successfully designed flapping wing from the Wright State University Center for Micro Air Vehicle Studies was employed as the benchmark for other design trials. The details about the whole system and flying test can be found in Hsu et al. (2010). The original design of the wing is made of PET of a thickness of 35 μm. It has a chord length of 72 mm, a whole wing span of 190 mm, and a cross strut pattern of S1, as shown in Fig. 3. In the present study, three types of materials, three chord lengths, three span sizes, and three cross strut patterns were carefully selected to make the test matrix.

3.3 The effects of flexible wing materials on the thrust generation for static flapping test

The first parameter to be examined is the effect of membrane material for the wing of the identical dimension (c=87 mm, s=190 mm). The parameters of three test wings have been tabulated in Table 1. Three types of materials have different thickness and different density, and thus different weight. In the first test round, the four-wing flapper was mounted on the load cell without wind, which is named the static flapping test. This experiment can be utilized to determine the ability of thrust-generation for different wing designs. During this test, the four-wing flapper was mounted with a zero angle of attack (AOA). The performance of the wings has been demonstrated in terms of the ratio of thrust to weight versus flapping frequency and power consumption, respectively, as shown in Fig. 5(a) and Fig. 5(b). The ratio of the thrust to the weight of the wing is chosen as the parameter for comparison, which is based on an analogy that the flapping wings serve as the "engine" of the aircraft, i.e. the MAV. It is well known that the thrust to weight ratio is the most significant parameter for an aeroengine.

It can be observed from Fig. 5(a) that the ratio of the thrust to weight for all wings increases as the flapping frequency increases, but with a different increase ratio. The worst performance was observed for the design with Latex with a thickness of 152 μm, which is the thinnest one found in the market. It might be noticed that the flapping test data for the latex wing only reaches up to 6 Hz. This restriction is mainly due to the insufficient ability of the power input and the insufficient tolerance of the mechanical system. The whole system cannot afford the inertial force of the latex wing at high frequencies, as the weight is much higher than the other two wings. The aluminized Mylar wing works slightly worse at low frequencies, but it works much better at high frequencies than the PET wings in terms of the ratio of thrust to weight. In the current design, the flapping frequency for the cruising flight is around 15 Hz. Fig. 5(b) shows the change of the ratio of thrust to weight with the increase of power input. Since the frequency of the flapping wing is controlled by the input power, i.e. voltage and current, the plots show a similar trend. The aluminized Mylar wing generates a higher ratio of thrust to weight with the same power consumption. From this point of view, Mylar seems the best choice for the current design. It should be noted that the weight of the aluminized Mylar wing is about 57% of the weight of the PET wing. The ratio of thrust to weight of the Mylar wing is around 30% higher than that of PET wing. This indicates that the identical sized PET wing generates higher thrust force than the aluminized Mylar wing, though the latter one has better thrust to weight ratio.

Table 1 Parameter for the material test

Material	Area (cm^2)	Thickness (μm)	Density (g/cm^3)	Strut pattern	Weight (g)
PET	138.71	35	1.38	S1	0.670
Mylar (Aluminized)	138.71	20	1.39	S1	0.385
Latex	138.71	152	0.94	S1	1.982

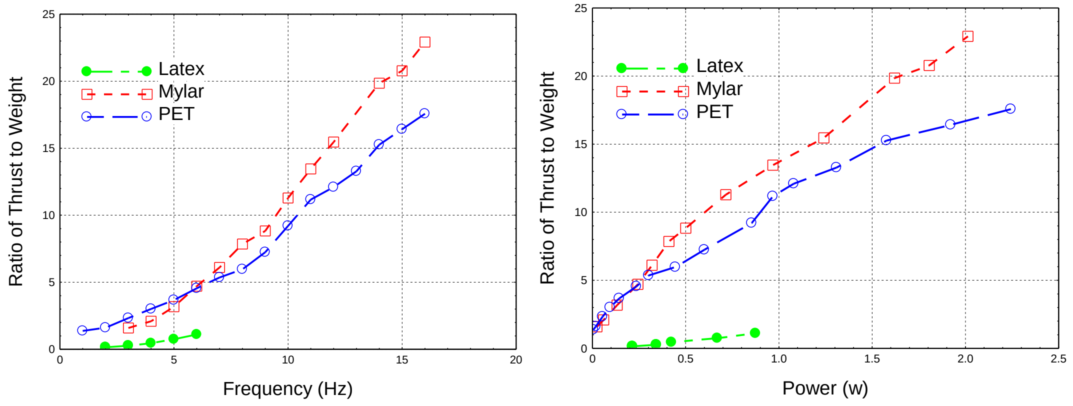

(a) Ratio of thrust to weight vs. flapping frequency (b) Ratio of thrust to weight vs. power consumption

Fig. 5 Comparison of the ratio of thrust to weight for different materials

For the practical MAV design, the weight of the wing is only a small part of the whole weight. The whole weight of the MAV, including all struts, tails, battery, and control elements, for the current design is about 12 grams. Considering the ratio of thrust to the whole weight of the MAV, PET is still the optimum choice for the current design. Meanwhile, the fragility and loud flapping noise of the aluminized Mylar wing restrict its wide applicability in the real MAV design.

3.4 The effects of wing dimension on the thrust generation for static flapping test

The second parameter to be examined is the wing dimensions. The test matrix is summarized in Table 2. The first three wings have the same spanwise length with varying chord length, i.e. c=72 mm, c=87 mm and c=80 mm. The remaining two wings have the same chord length of 80 mm with varying spanwise length of 270 mm and 350 mm. All these wings are made of PET with a cross strut pattern of S1. Again the test results were demonstrated in terms of the ratio of thrust to weight versus flapping frequency and power input as shown in Fig.6 and Fig.7. Fig. 6(a) depicts the ratio of thrust to weight varying with frequency for different chord length. As mentioned above, the cruising flapping frequency is about 15 Hz, thus attention should be drawn into the region around 15 Hz. It seems the wing with c=80 mm generates slightly higher thrust compared to those with c=72 mm and c=87 mm at the same flapping frequency. But the advantage is not distinguishable. Since the wing chord length increases, the power requirement increases in order to achieve the same flapping frequency. In Fig. 6(b), it can be clearly observed that the wing with c=87 mm consumes more power with the same generation of thrust to weight ratio because of the increase of chord length. The wing with c=72 mm performs slightly better than the wing with c=80 mm, but the difference is not outstanding. In summary, the variation of chord length in a small range does not show a distinguishable effect on the ratio of thrust to weight.

Table 2 Parameters for different wing sizes

c (mm)	**s (mm)**	**Strut pattern**	**Area** (cm^2)	**Weight (g)**
72	190	S1	117.44	0.567
87	190	S1	138.71	0.670
80	190	S1	127.89	0.618
80	270	S1	189.15	0.914
80	350	S1	246.22	1.189

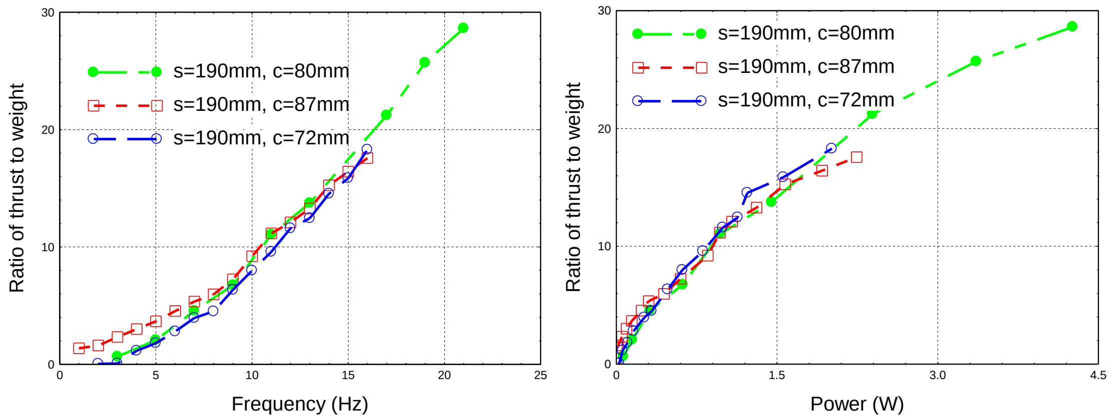

(a) Ratio of thrust to weight vs. flapping frequency (b) Ratio of thrust to weight vs. power consumption

Fig. 6 Ratio of thrust to weight for different chord length of wings

Fig. 7(a) shows the ratio of thrust to weight varied with different span size. The difference becomes much more distinguishable. Due to the limited power input and structure tolerance, the flapping frequency for s=350 mm can only reach up to 11 Hz. Definitely, a bigger size in the spanwise of the wing results in a higher ratio of thrust to weight in the low frequency region. But after 15 Hz, the thrust to weight ratio of the wing with s=270 mm jumps down and gets very close to the curve of the wing with s=190 mm. This interesting phenomenon might be attributed to the very large nonlinear deformation of the long flapping wing at high frequencies. On the other hand, as shown in Fig. 7(b), the larger span size requires more power input to maintain the same flapping frequency. Combining the concerns with both the ratio of thrust to weight at frequency around 15 Hz and power efficiency, the wing with spanwise length of 190mm and chord length of 80mm was determined as the optimum in current design, given the limit on the power supply and endurability of structures.

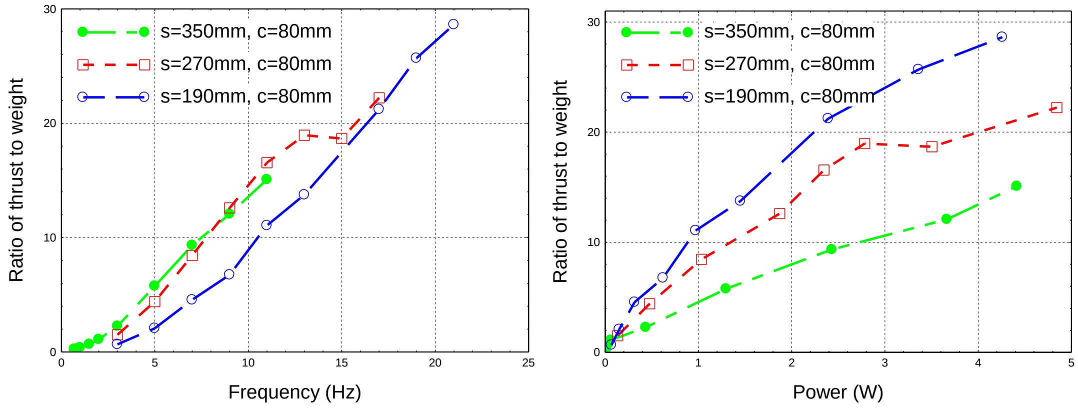

(a) Ratio of thrust to weight vs. flapping frequency (b) Ratio of thrust to weight vs. power consumption

Fig. 7 Ratio of thrust to weight for different span of wings

3.5 The effects of strut pattern on the thrust generation for static flapping test

The third parameter to be examined is the cross strut pattern of the wing. The three cross strut patterns have been presented in Fig. 3. All three wings are made from PET with chord length of 80 mm and span of 190 mm, which is selected as the optimum from the above studies. The cross strut pattern S1 serves as the original design for the MAV. The cross strut pattern S2 and S3 has one more strut added to the original S1 wing at 30^o and 5^o, respectively. Fig. 8(a) shows the ratio of the thrust to weight versus frequency with different cross strut patterns. It is clearly observed that the cross strut pattern S2 produces the best ratio of thrust to weight at the same flapping frequency. It is believed that the addition of the strut improves the elasticity distribution and thus the aerodynamic performance of the wing when flapping. The deviation becomes more distinct for higher flapping frequencies, which is close to the cruising flight frequency. The strut pattern S3 produces the worst thrust to weight ratio, though, with an additional strut on the wing. This indicates that the position of the additional strut instead of the addition itself plays a very important role in the thrust to weight ratio. Fig. 8(b) shows the ratio of the thrust to weight with respect to the power consumption. In the low frequency region, it seems the strut pattern S2 consumes less power for the same thrust to weight ratio. However, in the higher frequency region, the strut pattern generates the best thrust to weight ratio with the same power input, which is mainly due to the weight difference of the wing. There is no surprise that strut pattern S3 produced the worst performance with respect to the power consumption, which indicates that an inappropriate addition of a strut could impair the aerodynamic performance of a flapping wing. Even though strut pattern S2 consumes a little more power, it is still selected as the best strut pattern in the present study. It should be noted that there might a great chance to find a better strut pattern if ones try more different positions of the additional strut or more struts.

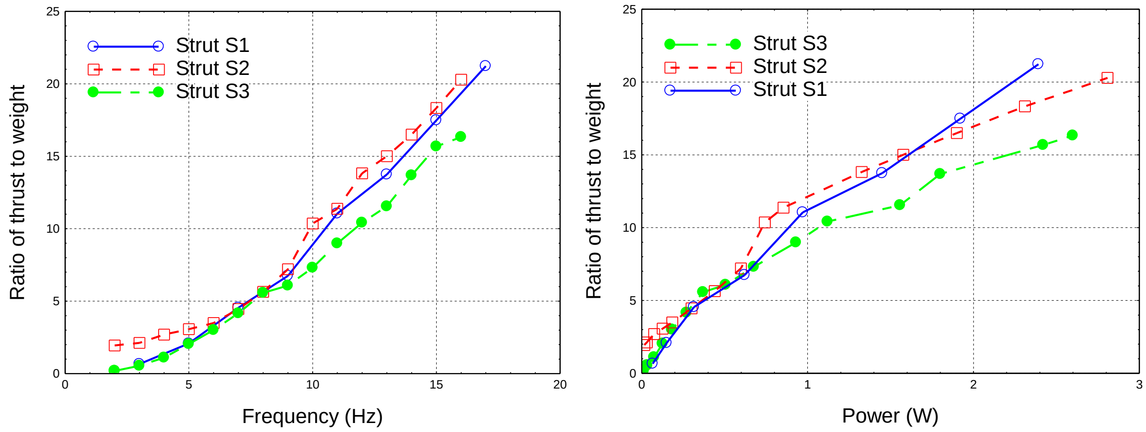

(a) Ratio of thrust to weight vs. flapping frequency (b) Ratio of thrust to weight vs. power consumption

Fig. 8 Ratio of thrust to weight for different strut patterns of wings

3.6 The effects of the strut pattern on the aerodynamic forces of flapping wings with incoming flow

In an effort to provide more realistic aerodynamic performance of the wing in flapping flight, the aerodynamic force data were acquired in a wind tunnel experiment with a uniform flow. The cruising flight speed of the MAV was determined to be between 2m/s and 3 m/s, with an AOA range from 40^o to 50^o via a free flight test. The flapping frequency is around 15 Hz. The test data were chosen as the parameter to conduct the wind tunnel experiments. Two wings are used in this experiment. One is the benchmark wing used for MAV with a chord length of 72 mm, spanwise length of 190 mm and cross strut pattern S1, named Wing I. The other one is the optimum wing based on the above studies with a chord length of 80 mm, spanwise length of 190 mm and cross strut pattern S2, named Wing II.

Fig. 9(a) and (b) show the time history of the thrust force with respect to the flapping phase angle for Wing I and Wing II with the incoming flow of 3m/s at an AOA of 50°. They show both original signal and filtered signal. The blue circles represent the PIV test points. The black curve represents the original signal. One can observe that a lot of noise is involved in the signal, which is mainly attributed to the vibration of the support rod for the flapping wings. A low frequency filter from matlab was applied. The red curve represents the filtered signal through using a low pass filter function on the original signal. Therefore, all signals above 100 Hz are filtered out. The filtered signal with smaller amplitude is believed to fairly present the temporal behavior of the thrust and lift generation during a complete flapping cycle. The phase angle shown in the plots were determined based on the data collected and analysis on the mechanism of the force generation. This analysis needs to be verified in the following synchronized measurement. In the present study, the phase angle 0° represents the position of totally clapped two wings as shown in Fig. 12(c); phase angle 180° represents the position of totally fling open wings as shown in Fig. 12(f). It can be observed that the maximum thrust was observed at phase angle of 0°. As the two wings start to fling, the thrust decreases substantially to a minimum at around 50° of the phase angle. The thrust rebounds to a high value at around 100° and then drops again to the minimum at around 150° to 180°. After reaching the fling open position at 180°, two wings start to clap and reach another peak thrust at around 240° to 250°. The thrust reaches another minimum value at around 300° and then returns to the maximum at the totally clapped position at around 360°. Comparing the thrust in a cycle for Wing I and Wing II, there is no distinct difference in the temporal behavior and averaged value but an outstanding difference in the amplitude of the oscillation.

Fig. 10(a) and (b) show the time history of the lift force with respect to the flapping phase angle for Wing I and Wing II with the incoming flow of 3m/s at an AOA of 50°. It can be observed that the discrepancies of the temporal behavior for the two wings are not quite obvious. For Wing I, the maximum was found at 0° (i.e. 360°) and 180°; the minimum was found at 60° and 300°. For Wing II, the maximum was found at 0° (i.e. 360°) and 180°, which is the same as Wing I. The minimum was found at 120° and 300°. The slight difference lies in the range from 30° to 150°. Another point deserving notice is that the amplitude of the lift for every phase angle for Wing II is slight higher than that for Wing I, which is confirmed by the averaged lift curve in Fig. 12(c). It has to be noted that the high frequency vibration induced outstanding variation of the amplitude. While the filter function is applied, the considerable effect of the filter might induce errors on the thrust and lift curve shown in Fig. 9 and Fig. 10. The thrust and lift curves also slightly vary from cycle to cycle. Typical results were arbitrarily selected to present in this report.

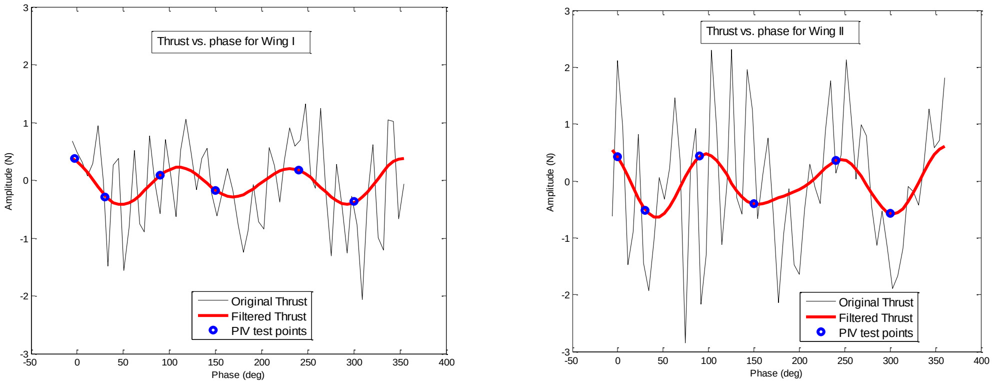

(a) Wing I (b) Wing II

Fig. 9 Thrust force in a flapping cycle for a. Wing I and b. Wing II

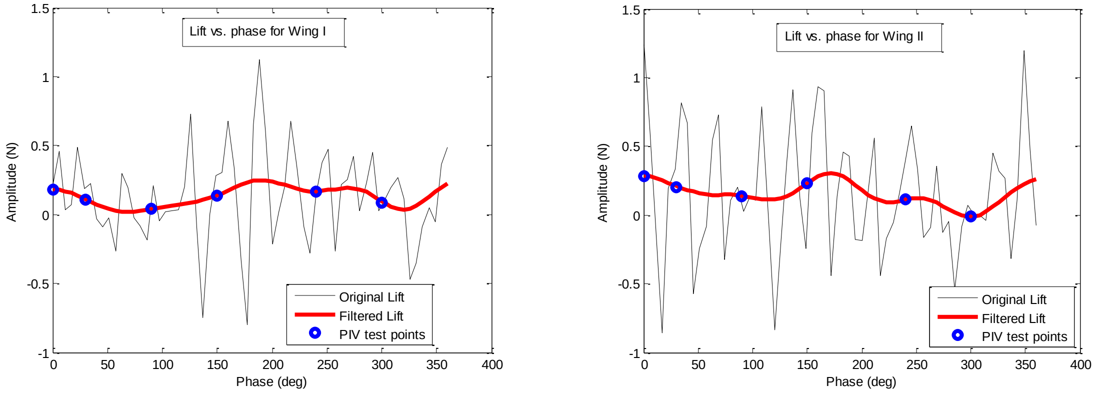

(a) Wing I (b) Wing II

Fig. 10 Lift force in a flapping cycle for a. Wing I and b. Wing II

In order to get rid of the vibration noise effect, the average thrust and lift value were statistically calculated and presented in Fig. 11. All thrusts presented in Fig. 11 are the net force in the x direction. Fig. 11(a) shows the thrust and lift coefficient varying with different flapping frequency at an AOA of 10 degrees with the incoming flow of 2m/s. This is not a situation that the flapper experienced during a cruising flight, but might be experienced during a transition. Generally, both the lift and thrust coefficients increase with flapping frequency. Wing II with strut pattern S3 performs better than Wing I with strut pattern S1, which agrees with the static force test results shown in Fig. 8(a). Compared with other two cases in the Fig. 11(b) and Fig. 11(c), large and positive thrust coefficients were generated; meanwhile, a substantial reduction of lift coefficients was observed. Fig. 11(b) shows the lift and thrust coefficients at AOA of 40 degrees with the incoming flow of 2m/s. Positive thrust coefficients were observed for the flapping frequency above 15 Hz. A slightly higher thrust coefficient was obtained for Wing II. But increase of lift coefficient for Wing II compared with Wing I becomes distinct. The difference becomes less distinct for the case at AOA of 50 degrees with the incoming flow of 3.0 m/s as shown in Fig. 11(c). The thrust coefficient for Wing II presents a higher value than that of Wing I, but both wings show negative values for the whole range of flapping frequencies. This indicates that the flapper cannot make the cruising flight at this AOA with the speed of 3m/s, even though this situation was observed in the flight test of the MAV. This discrepancy may lie in the fact that the MAV only flies with a speed of 3 m/s at AOA of 50^{o} transitionally during the flight test. The other reason for this discrepancy might be attributed to the measurement uncertainty in the AOA and flight speed. The uncertainty of the AOA measurement and flight speed measurement is estimated to be ±2^0 and ±0.5 m/s respectively.

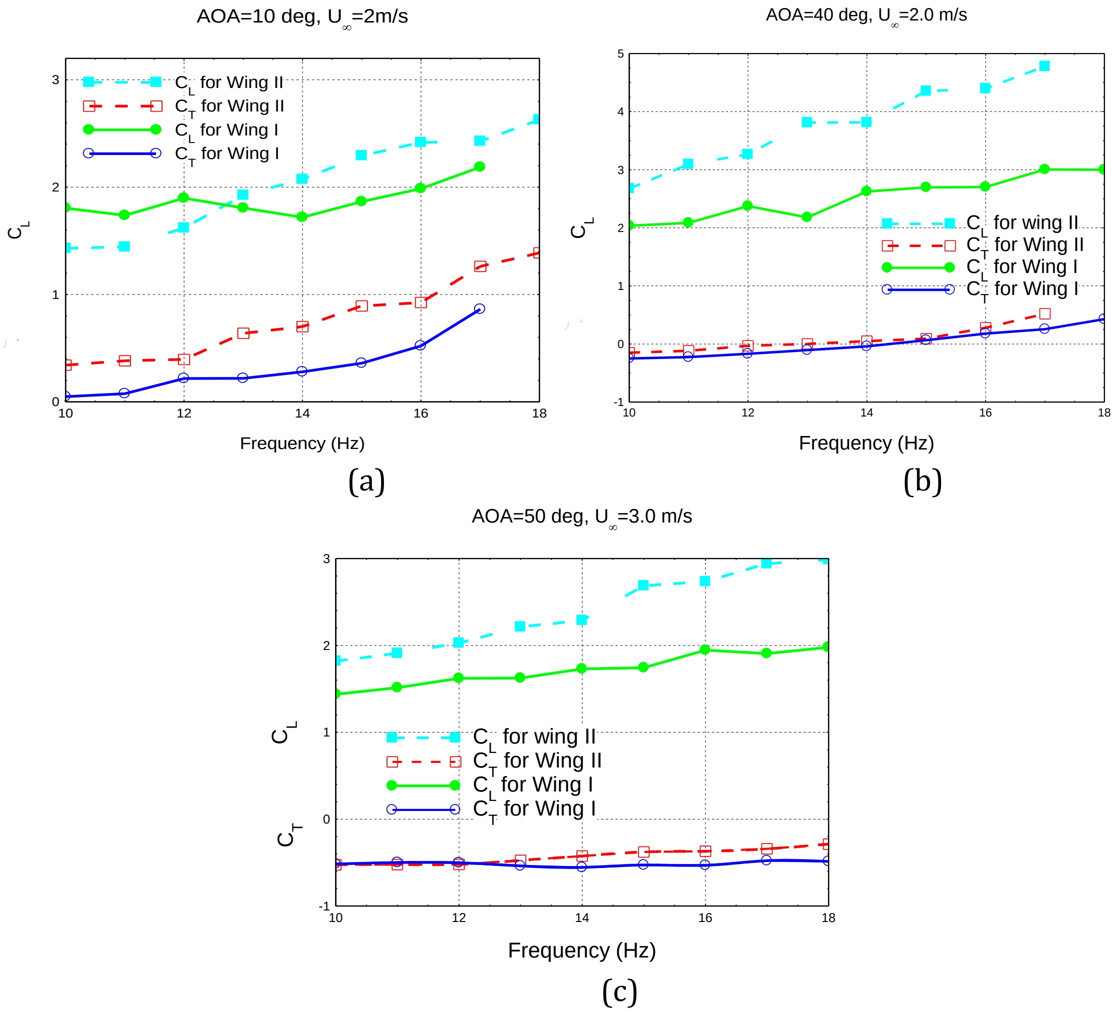

Fig. 11 Averaged thrust and lift coefficient at different flapping frequencies: (a) AOA=10 deg, U_∞=2m/s; (b) AOA=40 deg, U_∞=2m/s; (c) AOA=50 deg, U_∞=3m/s

3.7 The effects of the strut pattern on the flow characteristics of flapping wings

One of the most noticeable effects of having a flexible wing was that the wing flexed such that the wingtip generally lagged the wing root (Massey et al, 2009). The schematic feature of the flexible wing motion has been displayed in Fig. 12. This figure shows the section schematic of wings approaching each other to clap (a-c) and fling apart (d-e). Black lines present flow streamlines, dark blue arrows show induced flow, and the red arrows show net forces acting on the wing section. As the two wings approach each other dorsally as shown in Fig. 12(a), their leading ledges touch initially as shown in Fig. 12(b), and the wing rotates around the leading edge. As stated by Shyy (2010), vortices shed from the trailing edge roll up in the form of stopping vortices and dissipate into the wake when the trailing edges approach each other as shown in Fig. 12(c), which corresponds to the phase angle of zero as aforementioned in the force measurements. Meanwhile, the leading edge vortices also lose strength. The closing gap between the two wings pushes air out, giving a substantial additional thrust (Sane, 2003). The clapping motion is followed by fling motion. The wings fling apart by rotation around the trailing edge as shown in Fig. 12(d). The leading edge translates away, and air rushes in to fill the gap between the two wing sections, giving an initial boost in circulation around the wing system as shown in Fig. 12(e). A leading edge vortex forms anew, but the trailing edge starting vortices are mutually annihilated as they are of opposite circulation as shown in Fig. 12(f). As originally described by Weis-Fogh (1973), this annihilation may allow circulation to build more rapidly by suppressing the Wagner effect. These descriptions were confirmed by the PIV measurements presented below.

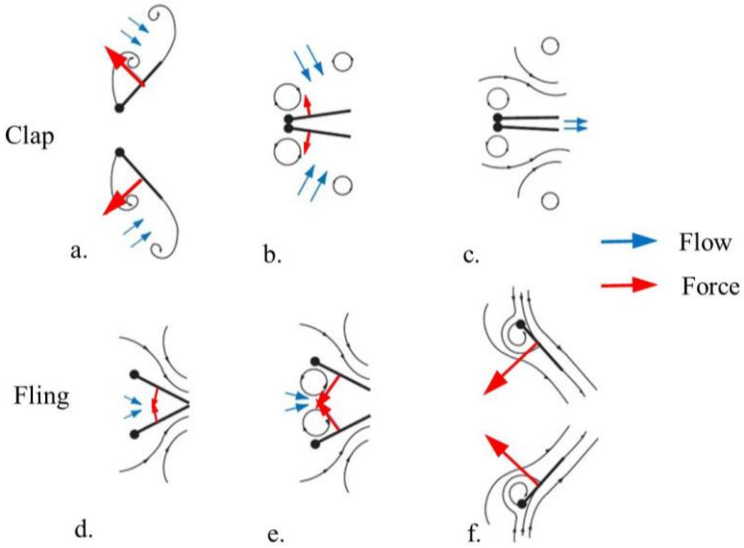

Fig. 12 Clap and fling motion of the two wings

In an effort to provide a deeper understanding of the fluid dynamics of the flapping wing, phase-locked PIV measurements were conducted to provide detailed flow field information. In the PIV measurements, the flapper was installed in the wind tunnel at an AOA of 50 degrees with a uniform flow velocity of 3m/s. Six phase angles fairly corresponding to peak and valley points in the temporal thrust curve, shown as the blue circles in Fig.9 (a) and (b), were carefully selected as the PIV test points. Fig. 13 shows the PIV measurement results in terms of phase-locked averaged velocity and vectors around the left pair of wings (facing incoming flow direction) in a cross plane at the half span of the wing (i.e. z = 47.5 mm with respect to the center line of the MAV). It is noted that the two-dimensional wing shape data at different phase angles was extracted from the PIV raw image and plotted in the plots. Even though measurements on one cross plane cannot tell the whole story of the flow around the flapping wings, it could be used to describe the essential vortex flow characteristics to some extent. Fig. 13(a), (c), (g) and (k) show the velocity field at phase angles of 0°, 30°, 90°, and 150° respectively for Wing I. Fig. 13(b), (d), (h), and (I) show the velocity field at phase angles of 0°, 30°, 90°, and 150° respectively for Wing II. At the phase angle of 0°, i.e. the position as shown in Fig. 13(c), a “jet shape” flow with high velocity was observed downstream of the wings, which agrees with the flow pattern shown in Fig. 13(c). It is obvious that Wing II generates a stronger jet flow in terms of higher velocity and a larger affecting region than Wing I. This difference lies in the fact that the addition of one more strut at 30° on the wing, i.e. strut pattern S2, effectively strengthen the stiffness of the wing on the region of interest. The appropriate reinforcement on the stiffness results in a stronger ability to push the air out of the gap. Therefore a higher thrust as well as a higher lift for this phase angle was obtained as shown in Fig. 9 and Fig. 10. As the angle of attack for the PIV test is 50°, a strong downwash velocity component can be observed in the “jet shape” flow. Another point that deserves attention is that the flow stays attached to the upper surface of the wing in spite of the large AOA, because the flapping motion of the wing builds a strong lead edge vortex that helps to maintain an attached flow.

After two wings reach the completely clapped position (i.e. phase angle = 0^o), they start to fling open. As described above, the wings fling apart by rotation around the trailing edge. Thus, apart leading edges of wings were observed for the phase angle of 30^o, but trailing edges kept touching for both wings as shown in Fig 13(c) and (d). The high velocity “jet shape” flow travels downstream a bit at a phase angle of 30^o. The area of the high velocity region shrinks down, while Wing II still prevails in terms of higher velocity and larger affecting region. The flow above the upper surface remains attached for this phase angle. Since air starts to rush in to fill the gap between the two wings, the wings experience the first drop of thrust as shown in Fig. 9 (a) and (b). As the phase angle increases to 90 degrees, which corresponds to the fling position (g) in the Fig. 13, an initial boost in circulation around the wing system will be generated even though it cannot be seen from the PIV results. But one can observe that additional flow leaving the gap tends to feed the original jet flow and results in an increase of the thrust, which agrees fairly well with the temporal thrust curve shown in Fig. 9. As the phase angle increases to 150 degrees, with the two wings almost apart to a maximum angle, one has moved off the measurement plane. The reflection of the wing off the plane makes the particles invisible for the PIV measurements. However one can still observe the downwash right after the trailing edge of the bottom wing, which results in increased lift but a decreased thrust as shown in Fig. 9 and Fig. 10. Comparing the flow of Wing I with that of Wing II at each angle of attack, it is obvious that Wing II induced a much stronger flow, although the flow structure is similar. It should be noted that the change of the flow characteristics at different phase angles shown in the plots is also affected by the three-dimensional flow feature, which cannot be taken into account in the present 2D PIV measurement. Future work of this study will employ a stereoscopic PIV technique to address this issue.

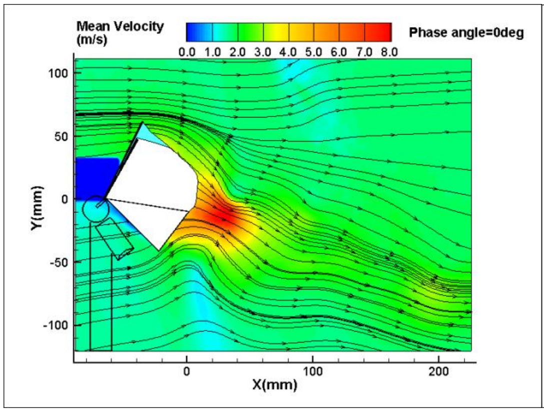

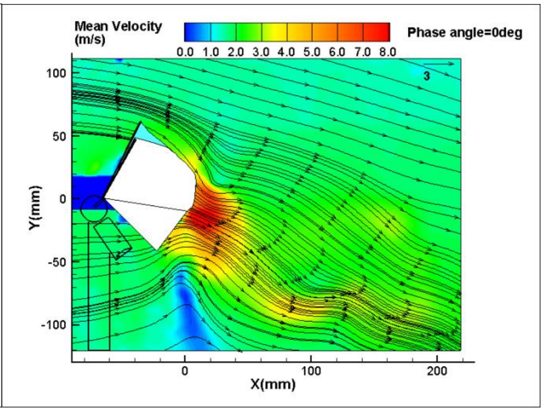

a).WingI b.)Wing II

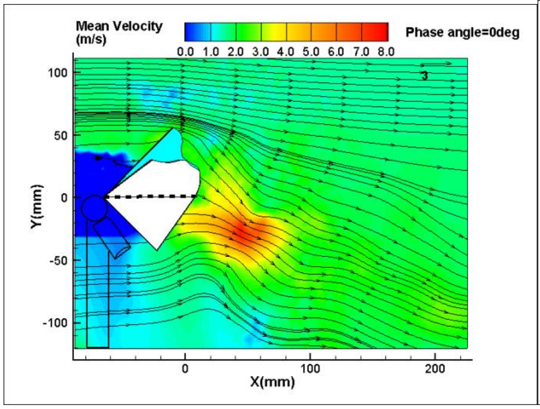

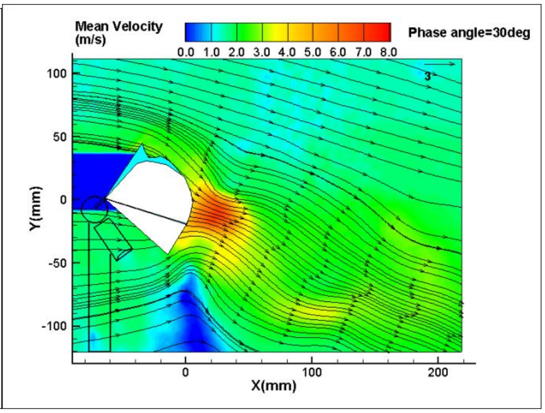

c.).WingI d.)Wing II

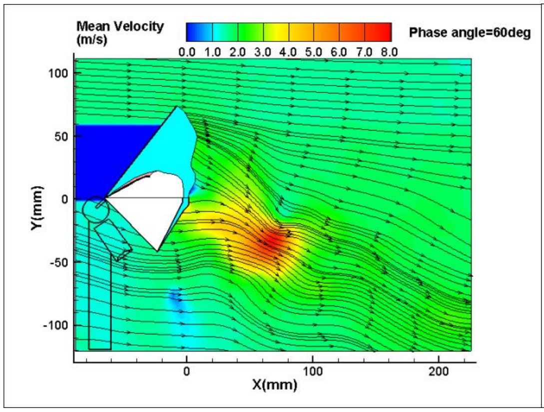

e.).WingI

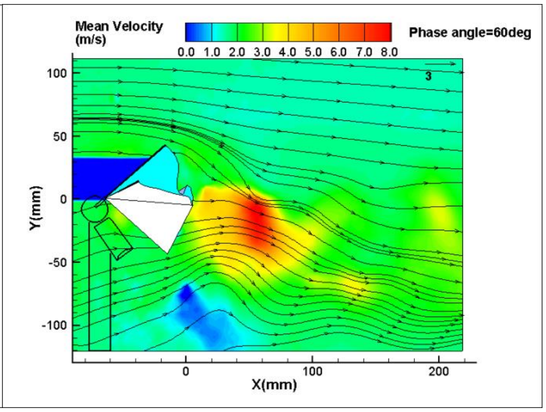

f.)Wing II

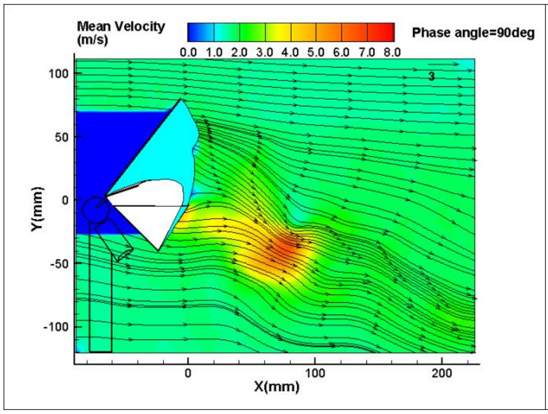

g.)WingI

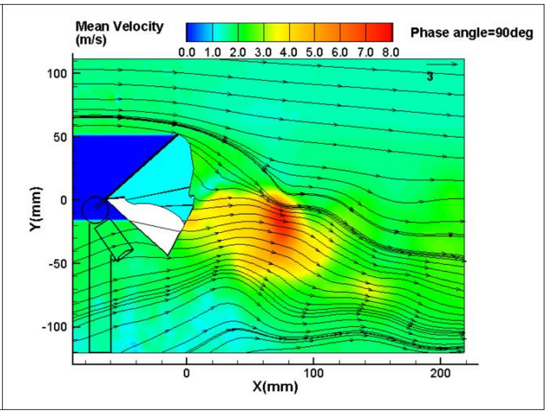

h.)Wing II

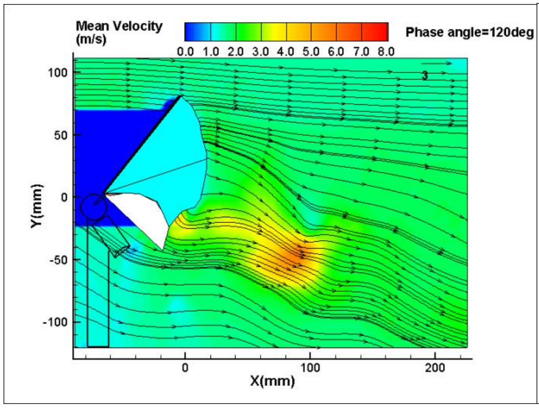

i.).WingI

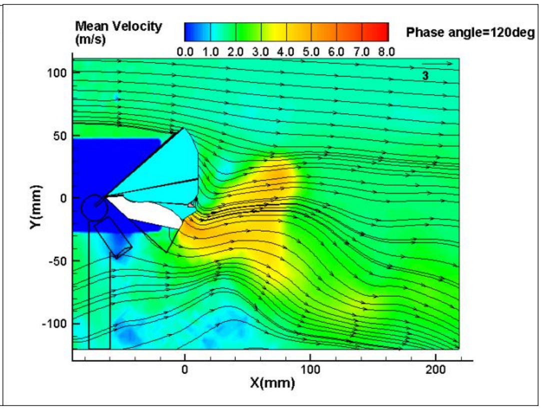

j.)Wing II

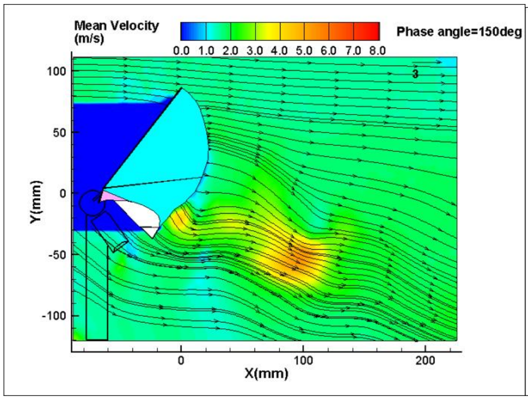

k.).WingI

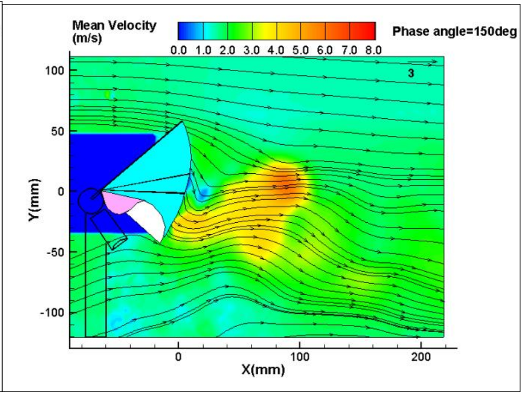

l.)Wing II

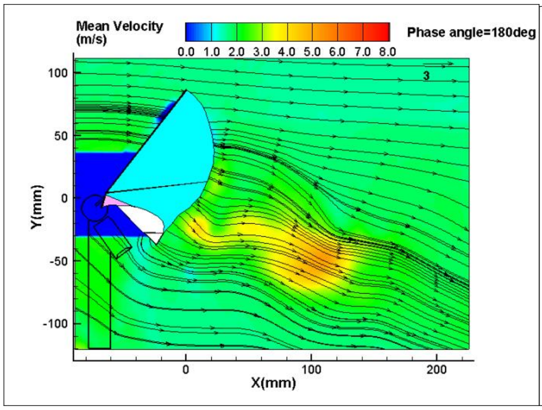

m.)WingI

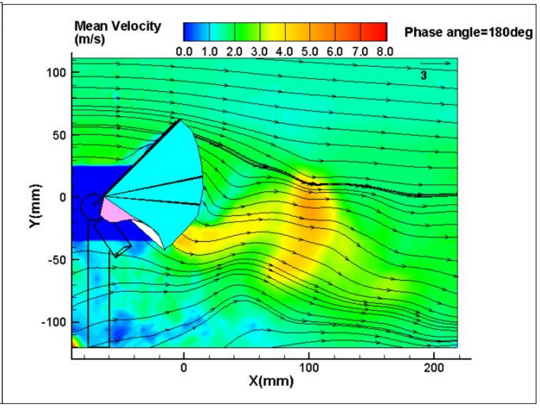

n.)Wing II

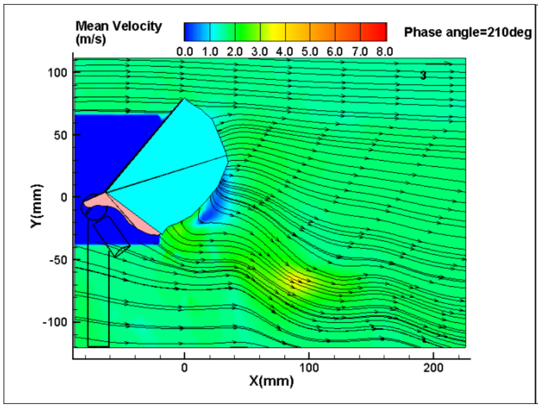

O.)WingI

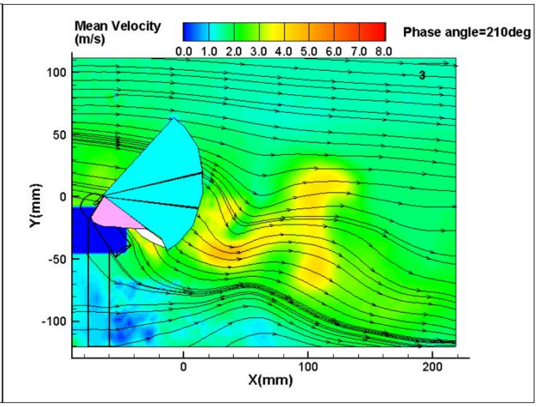

p.)Wing II

Fig. 13 Phase-locked averaged velocity distribution at different phase angles for fling open motion

Fig. 14 (a) and (b) show the flow field at a phase angle of 240^{o}, which corresponds to the position (a) in Fig. 12. The strong leading vortex cannot be observed in the present results because of the experimental setup and wing reflections. Due to the strong leading vortices, wings at this phase angle can produce a large thrust and fairly good lift, which can be seen in Fig. 9 and Fig. 10. Fig. 14 (e) and (f) show the flow field at a phase angle of 300^{o}, which corresponds to the position (b) in Fig. 12. The lead edge vortex effect becomes trivial. Low velocity regions appear in the downstream of the wings. The deformation of the wing prevents the generation of thrust and lift; thus the valley point in both temporal thrust and lift curves was observed in Fig. 9 and Fig. 10. All in all, comparing the flow of Wing I with that of Wing II at each angle of attack, it is obvious that Wing II induced a much stronger flow, although the flow structure is similar, which agrees with the finding in the force measurements.

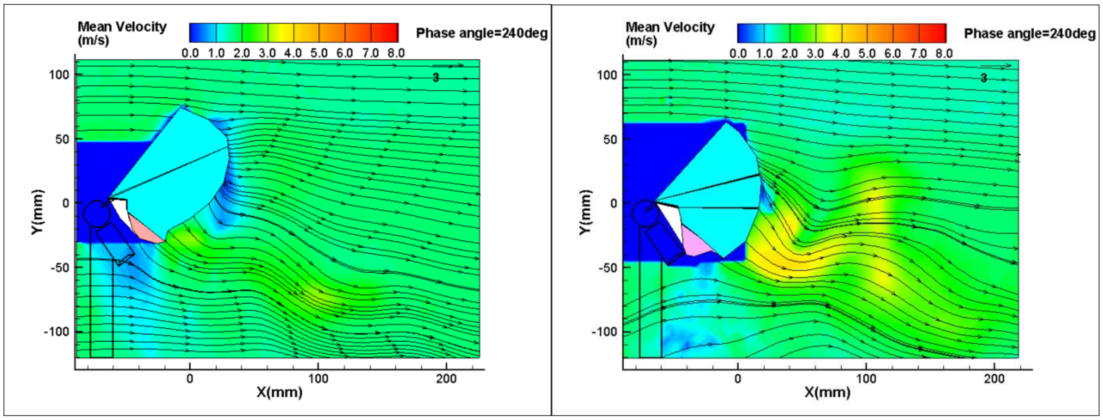

a.)Wing I

b.)Wing II

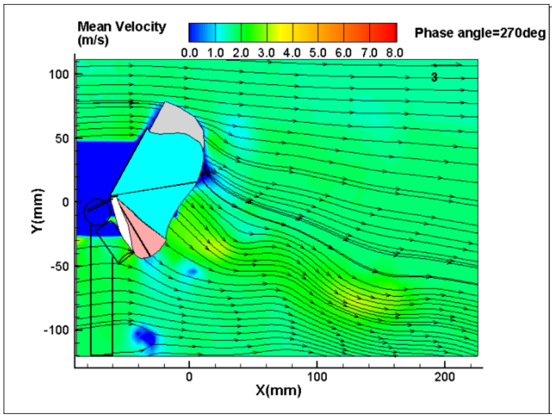

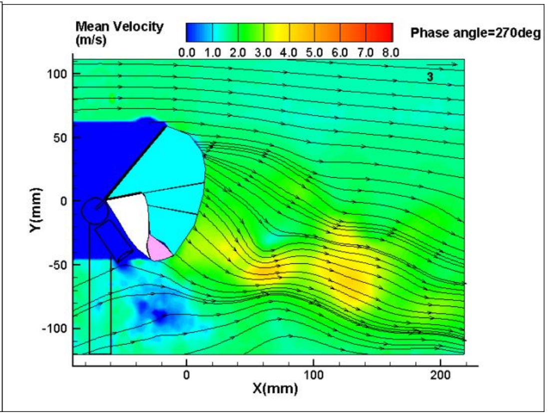

c.)Wing I

d.)Wing II

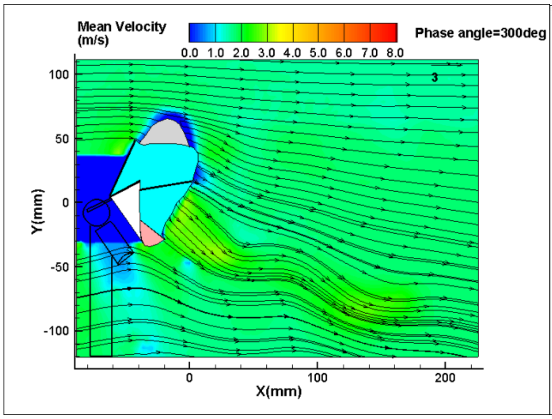

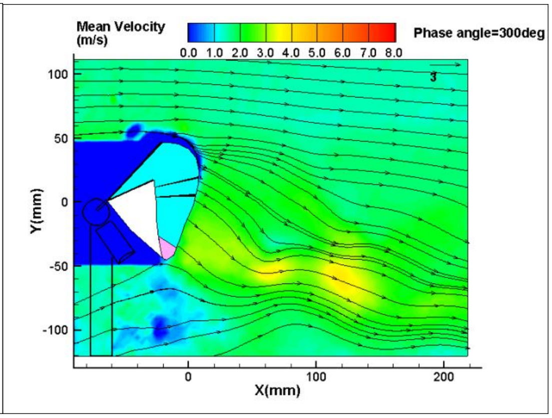

e.)Wing I

f.)Wing II

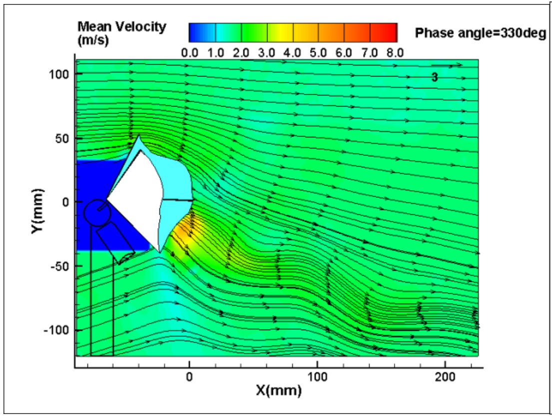

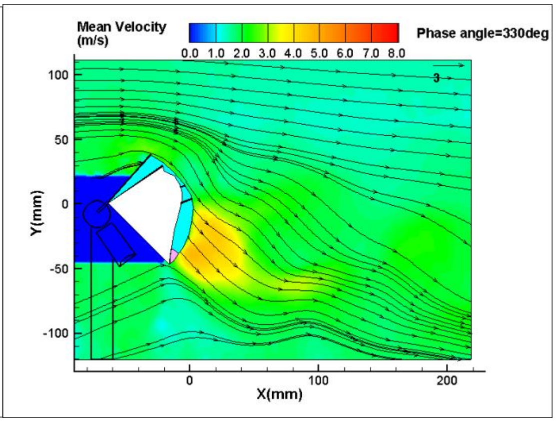

g.)Wing I

h.)Wing II

Fig. 14 Phase-locked averaged velocity distribution at different phase angles for clapping motion

In order to quantify the flapping induced flow, the uniform velocity was subtracted from the flow velocity distribution. Fig. 15 (a) and (b) show the flapping induced velocity at phase angle of 0^o for Wing I and Wing II, respectively. Wing II definitely induced a larger momentum of the flow downstream of the wings, which agrees with the observation from the mean velocity distribution above. After subtracting the incoming flow velocity, two distinct vortices can be observed clearly: one located below the “jet shape” flow, the other located above the “jet shape” flow. The one above the jet flow for Wing II is located slightly higher than the one for Wing I, which is mainly attributed to the change of flexibility distribution of the wing. Fig. 15 (c) and (d) show the flapping induced velocity at a phase angle of 150^o for Wing I and Wing II, respectively. It can be seen that the flow pattern for Wing II differs from Wing I significantly. At around x=175mm downstream of the wings, only one concentrated region with downwash is observed for Wing I. At the same location, flow tends to be bifurcated with both downwash and upwash for Wing II. The vortex structure is also quite different for these two wings.

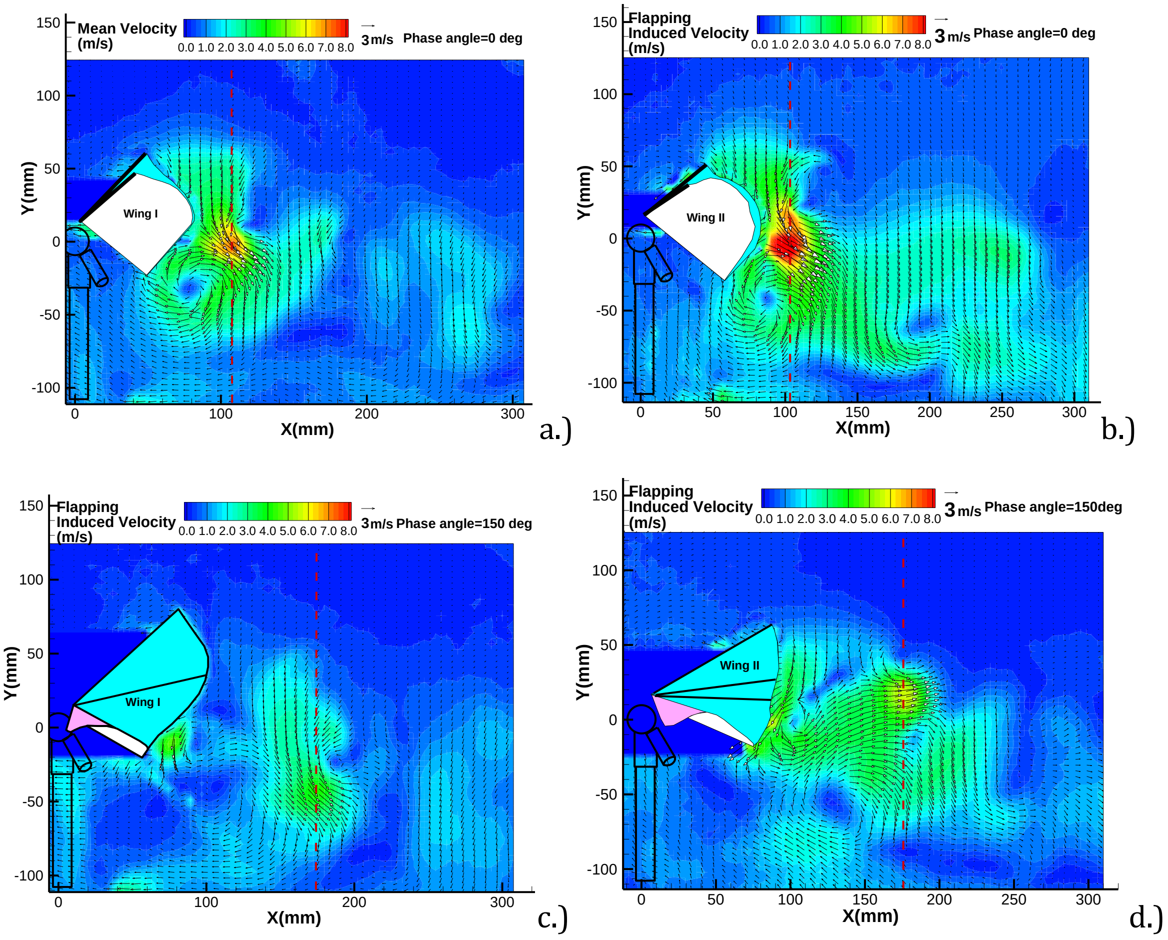

Fig. 15 Flapping induced velocity distribution at different phase angle

In an effort to provide a more detailed comparison of the induced velocity distribution, a characteristic location was selected for each case to extract a velocity profile for comparison. The locations for extraction of velocity profiles are illustrated as the red dash line in Fig. 15 (a), (b), (c) and (d). The velocity profiles are plotted and compared in Fig. 16 (a) and (b) for phase angles of 0^o and 150^o, respectively. For the case at a phase angle of 0^o, a similarity of the shape of the velocity profiles is observed, but Wing II generates a greater value of velocity at every elevation. For the case at a phase angle of 150°, the velocity distribution is very different for the two wings. Wing I presents the dominant peak of the mean velocity at y = -50 mm, while Wing II presents the dominant peak value at y = 20 mm. This indicates that Wing I and Wing II might generate different coherent structures of vortices due to the different cross strut pattern in the wing.

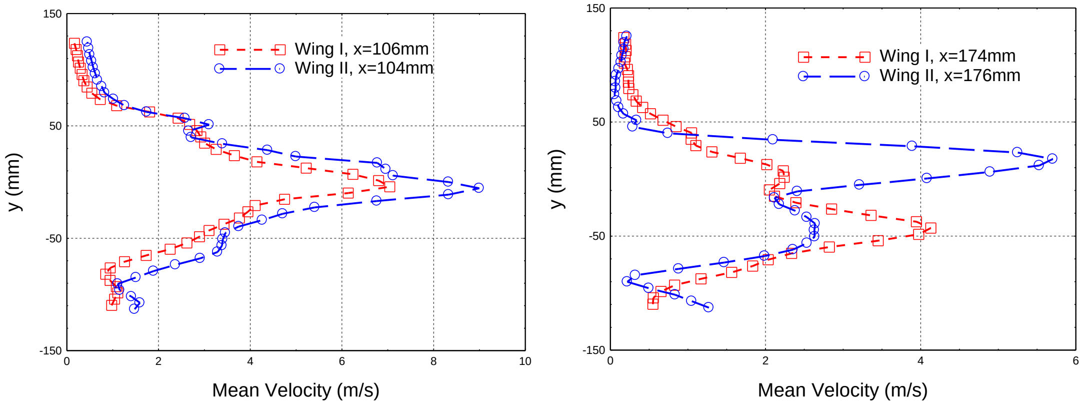

(a) phase angle= 0°

(b) phase angle =150°

Fig. 16 Profiles of the flapping induced velocity distribution at different phase angle

While the experimental setup limits the visibility of the vortices around the flapping wing, especially at some large phase angles, the vortices downstream of the flapping wings were clearly visualized and quantified in the mid-span plan, i.e. the vertical at z = 47.5 mm, as shown in Fig. 17 and Fig. 18. Fig. 17 (a) and (b) show the phase-locked averaged vorticity distribution at a phase angle of 0° for Wing I and

Wing II, respectively. The leading edge vortices are blocked by the wing, although negative vorticity appears around the upper wing, which is believed to be a fake vorticity. The velocity near the edge of wing cannot be calculated correctly from the PIV processing; therefore, the velocity gradient in the near region of the wing edges results in a fake vorticity region. It can be observed that two strong vortices with inversed rotation were generated downstream of the wing due to the strong jet flow from the gap. The bottom wing induces an upwash, which merges in the jet flow to produce a perfect vortex flow as shown in Fig. 17 (a) and (b). It seems the center for this vortex is slightly apart from the center of the vortex induced by the jet flow for both wings. As the phase angle increases, the two negative vortices for Wing II tend to separate. One moves downstream and upward, while the other one moves downstream and downward. The vorticity dissipates relatively slowly from a phase angle of 0^o to 150^o. But for Wing I, the two negative vortices tend to separate as well, in which one vortex lags the other and both of them move downstream and downward. The vorticity dissipate relatively quickly from a phase angle of 0^o to 150^o.

The vortex center of the positive vortex above the jet flow for Wing II differs from that for Wing I at phase angle of 0^o, which agrees with the observation in Fig. 17 (a) and (b). The positive vortex moves downstream and slightly upward for Wing II, while it moves downstream and downward for Wing I. As stated previously, this is because of the change of the flexibility distribution of the wing. As the two wings fling out, at the phase angle of 90°, the positive trail edge vortex (named secondary positive vortex) starts to form at the trailing edge of the bottom wing due to the fling motion. This positive vortex starts to shed at a phase angle of 150°. This positive vortex moves downstream and downward for both wings. It pairs up with the undissipated negative vortex to form another pair of vortices, which can be observed clearly near the bottom right in Fig. 17 (b). For Wing I, the location of the secondary positive vortex is far from the undissipated negative vortex, and they both dissipate quickly and thus cannot be observed easily from Fig. 17 (a). This secondary positive vortex can be observed clearly in Fig. 18 (a) and (c). In the clap motion for phase angles of 240° and 300°, the jet flow induced vortices are almost dissipated for both wings. The secondary positive vortex paired with the undissipated negative vortex becomes distinct. Again, Wing II generated a stronger secondary vortex than that of Wing I. Obviously the pattern of cross-struts has considerable effect on the characteristics of the coherent vortex structures downstream of the flapping wings.

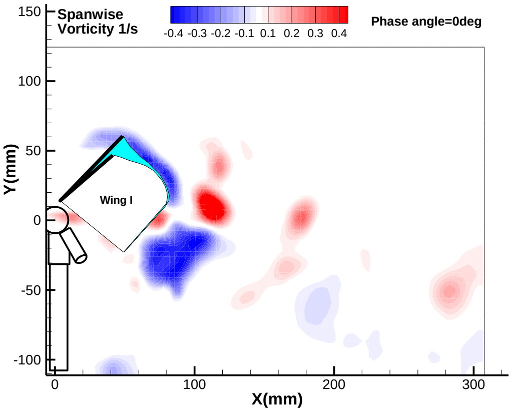
Spanwise
Vorticity 1/s
-0.4 -0.3 -0.2 -0.1 0.1 0.2 0.3 0.4
Phase angle=0deg
Wing I
150
100
50
0
-50
-100
Y(mm)
0
100
200
300
X(mm)

a.)

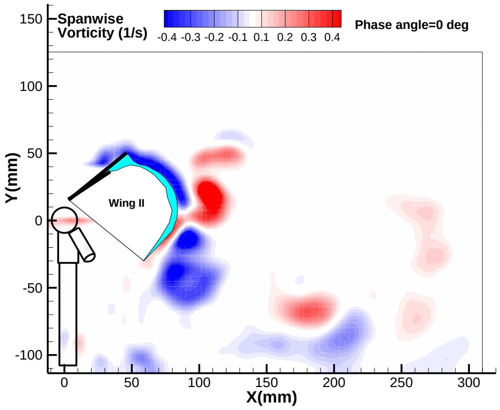
Spanwise
Vorticity (1/s)
-0.4 -0.3 -0.2 -0.1 0.1 0.2 0.3 0.4
Phase angle=0 deg
Wing II
150
100
50
0
-50
-100
Y(mm)
0
50
100
150
200
250
300
X(mm)

b.)

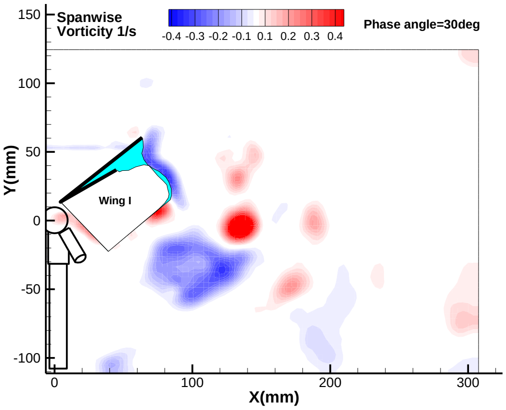
Spanwise
Vorticity 1/s
-0.4 -0.3 -0.2 -0.1 0.1 0.2 0.3 0.4
Phase angle=30deg
Wing I
150
100
50
0
-50
-100
Y(mm)
0
100
200
300
X(mm)

c.)

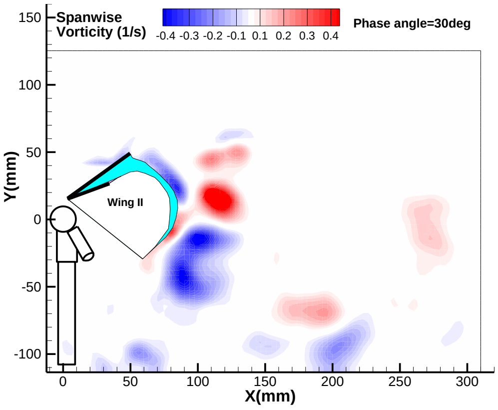
Spanwise
Vorticity (1/s)
-0.4 -0.3 -0.2 -0.1 0.1 0.2 0.3 0.4
Phase angle=30deg
Wing II
150
100
50
0
-50
-100
Y(mm)
0
50
100
150
200
250
300
X(mm)

d.)

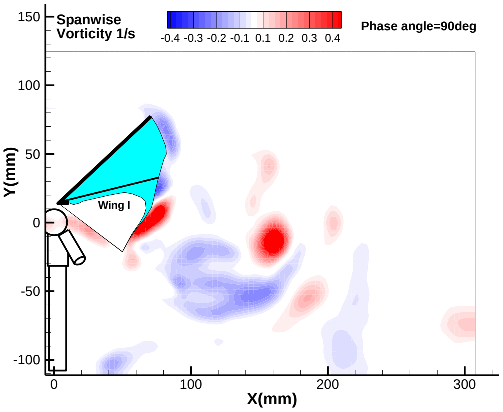
Spanwise
Vorticity 1/s
-0.4 -0.3 -0.2 -0.1 0.1 0.2 0.3 0.4
Phase angle=90deg
Wing I
150
100
50
0
-50
-100
Y(mm)
0
100
200
300
X(mm)

e.)

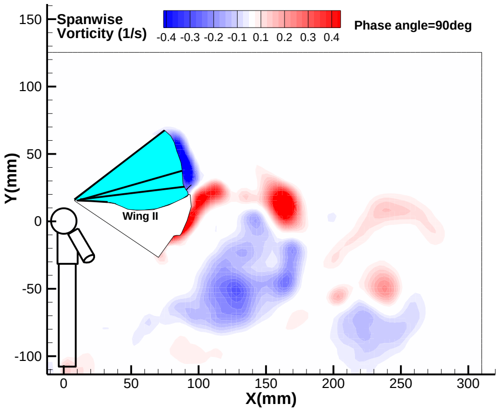
Spanwise
Vorticity (1/s)
-0.4 -0.3 -0.2 -0.1 0.1 0.2 0.3 0.4
Phase angle=90deg
Wing II
150
100
50
0
-50
-100
Y(mm)
0
50
100
150
200
250
300
X(mm)

f.)

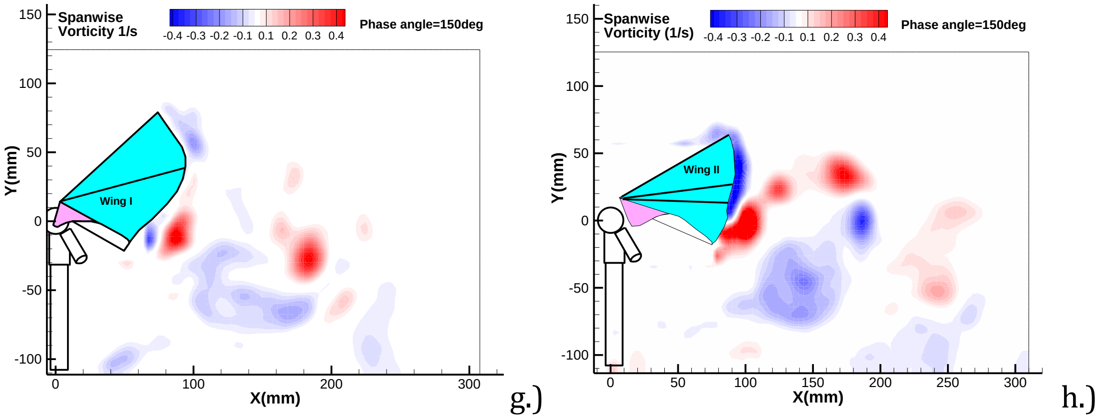

g.) h.)

Fig. 17 Phase-locked averaged vorticity distribution at different phase angles for fling motion

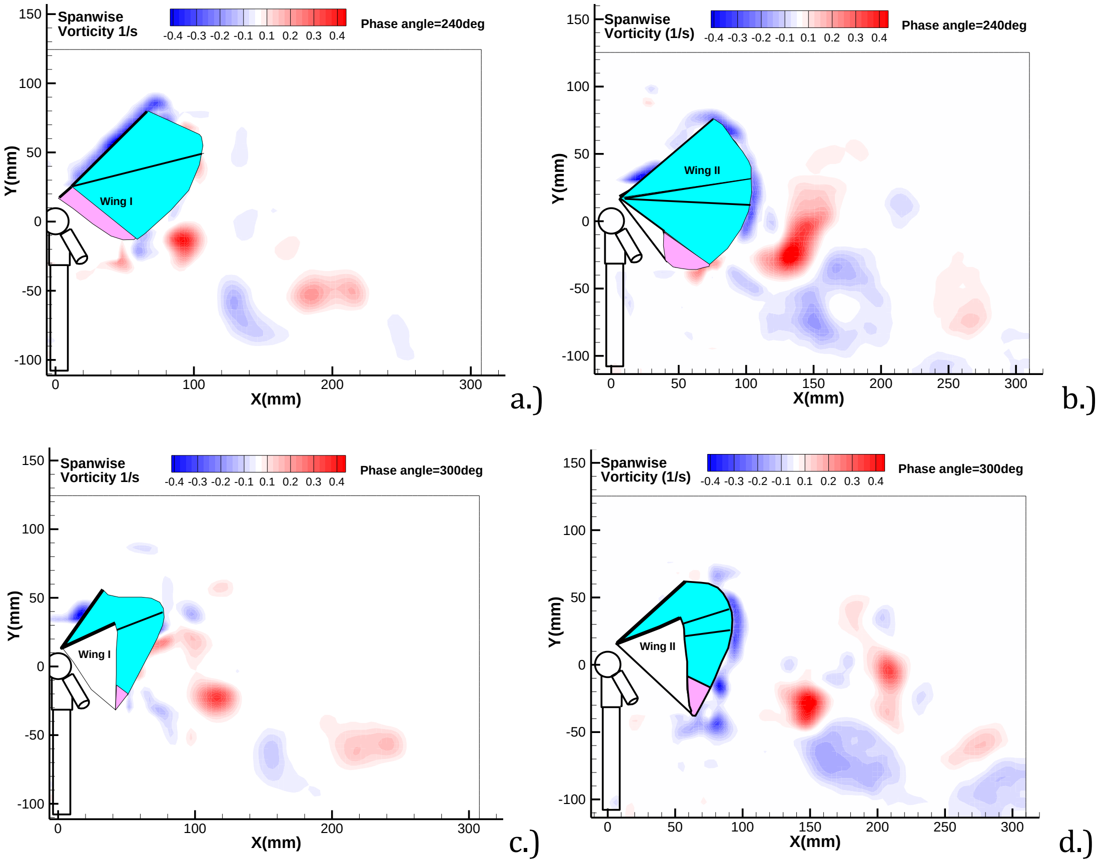

a.) b.)

c.) d.)

Fig. 18 Phase-locked averaged vorticity distribution at different phase angles for clap motion

3.8 Conclusion

An experimental study was conducted to investigate the flow characteristics of the flow around the flapping wings of a four-wing flapper as well as the lift and thrust coefficient of a four-wing flapper. In the present study, a clap-and-fling type of four-wing flapper was designed and manufactured by using several flexible materials, such as PET film, latex, and aluminized Mylar. Different cross-strut patterns and dimensions of wings were manufactured and tested for the optimization of wing designs. In addition to the lift and thrust measurements using two highly sensitive force moment sensor units, a high-resolution Particle Image Velocimetry (PIV) system was employed to achieve detailed flow field measurements to quantify the evolution of the unsteady vortex flow structure around and in the downstream of the flapping wings. The force measurements were analyzed in correlation with the detailed flow measurements to elucidate the underlying physics in order to improve our understanding for an optimized flexible wing design and better performance of the flapping wing MAV.

In the static flapping test on the force generation, it has been found that the aluminized Mylar performs best in terms of force generation as compared to PET film and latex with the same size and strut pattern. But the fragility and noise generation restrict the use of aluminized Mylar. Combining these concerns with both the ratio of thrust to weight at frequency around 15 Hz and power efficiency, the wing with spanwise length of 190 mm and chord length of 80 mm was determined as the optimum dimensions in the current design, given the limit on the power supply and endurability of the structures. The cross strut pattern in the wing plays in important role in determining the thrust to weight ratio. Even though strut pattern S2 consumes a little more power, it is still selected as the best strut pattern in the present study.

In the flapping experiment with incoming flow, the well selected Wing II, with a chord length of 80 mm, spanwise length of 190 mm and cross strut pattern S2, was compared to the original Wing I in every aspect of performance. The lift coefficient of Wing II increased drastically compared with Wing I; meanwhile, a slight increase of thrust was also observed. The force measurement data was analyzed, carefully correlating with the quantitative flow measurement using PIV. It was found that Wing II can generate higher momentum of the jet flow at the clapped position. During the whole clap-and-fling motion, it seems the flapping wing benefits from the improved flexibility distribution through adding one more skeleton at 30 degrees with respect to the leading edge of the wing. The coherent structures of the shedding vortices were also varied as the deformation of the whole wing varied for Wing II at each phase angle. The three-dimension characteristics of the vortex flow structure need to be addressed in future work using stereoscopic PIV techniques.

4. Aerodynamic Performance of Flapping Wings under Acoustic Disturbances

4.1 Experimental setup

The sound source located on the side of the flapper is a 38.1 cm diameter sub-woofer (PRV 15W1600 15''), connected to a 2000 W amplifier (Behringer EPX4000) and a function generator able to produce a pure tone. The amplifier output signals were monitored at the same time as both voltage and current by a 2 channel digital oscilloscope. The sound pressure level (SPL) was measured by a B&K ½ inch microphone connected to a B&K spectrum analyzer. The frequencies used in the present study are 21 Hz and 26 Hz. Although the function generator generates a pure tone signal, the actual sound generated by the loud speaker is not pure tone sound, especially for low frequency tones. As shown in Fig. 19 (a) through (d), the amplitude spectrum for the 21 Hz tone input and 26 Hz tone input with different amplifier gain values were measured and depicted. For the 21 Hz tone input, the maximum sound level was found at 63 Hz, which is the third harmonic of the 21 Hz. For the 26 Hz tone input with high gain value from the amplifier, the maximum sound level was observed at 78 Hz, which is also the third harmonic of the 26 Hz. But with the decreasing gain value (i.e. sound pressure level), the amplitude at 26 Hz becomes more dominant.

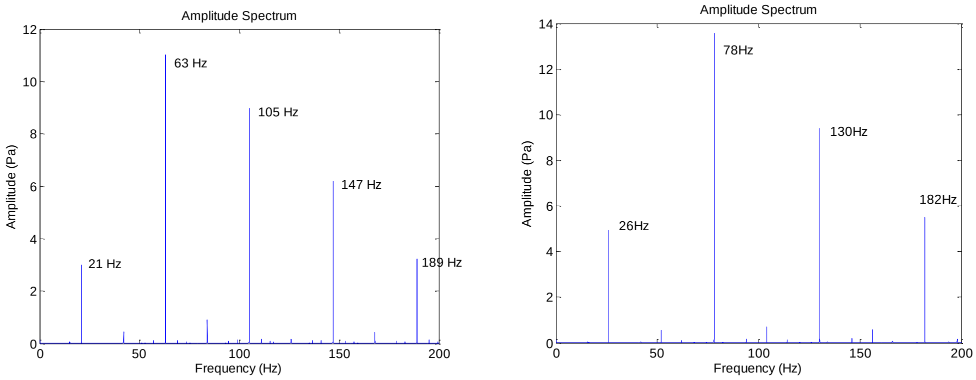

(a) 21 Hz sine input with tonal SPL=104dB (b) 26 Hz sine input with tonal SPL=107.9dB

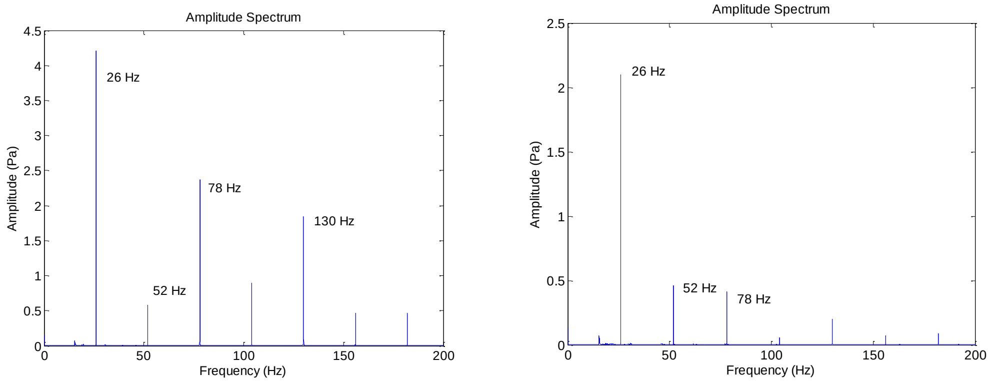

(c) 26 Hz sine input with tonal SPL=106.5dB (d) 26 Hz sine input with tonal SPL=100.4dB

Fig. 19 Sound pressure amplitude spectrum for different input tone and power level

The four wing flapper was connected through a supporting aluminum rod to a high-sensitivity force-moment sensor (JR3, model 30E12A-I40) in order to measure the dynamic wind load (both force and moment) acting on the wind turbine model. The JR3 load cell is composed of foil strain gage bridges, which are capable of measuring the forces on three orthogonal axes and the moment (torque) about each axis. The precision of the force-moment sensor cell for force measurements is estimated within ±0.025% of the full range (40N) according to the calibration. During the experiments, the wind loads data were acquired for 30 seconds at the sample rate of 2,000 Hz for each tested case.

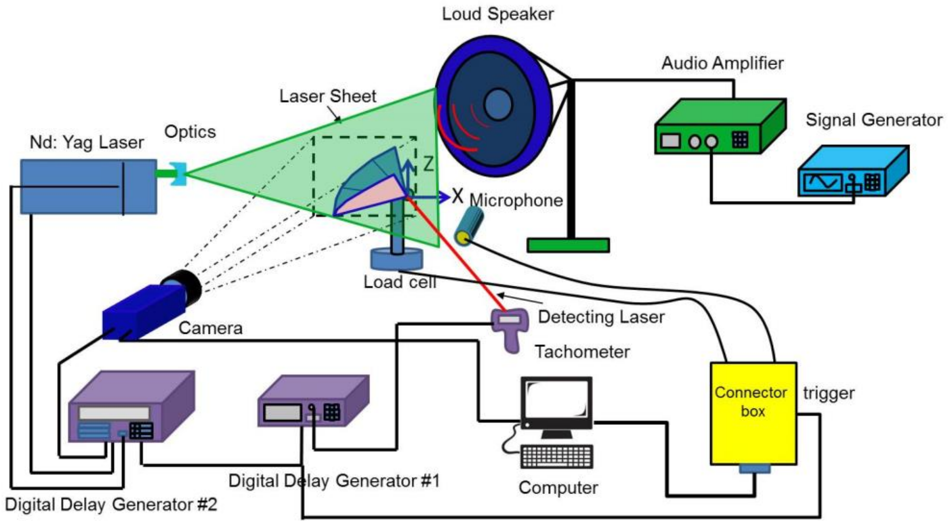

Fig. 20: Schematic of the experimental setup.

4.2 Results and discussions

As forementioned, a successfully designed and manufactured four-wing flapper from the Center for Micro Air Vehicle Studies in Wright State University was employed as the testbed for the effect of acoustic disturbances. The aerodynamic forces and flow field around wings for the four-wing flapper were measured using the load cell and a digital PIV system, respectively. Then the effect of acoustic disturbances on the aerodynamic forces and flow field were studied in comparison with the original undisturbed measurement results. During the test, the flapper was fixed on an optic table without any incoming flow. The angle of attack (i.e. pitch angle of the body) was set at 50 degrees, which is close to the angle of hovering. The loudspeaker was set at the side of the flapper with a distance of 14.5 inches from the center of the loudspeaker to the center of the gear of the flapper as shown in Fig. 20.

4.3 Effect of acoustic disturbances on aerodynamic forces

The averaged thrust, lift, and side forces are summarized in Table.1. The thrust force for all cases is around 0.06 N. The lift force is about 0.06 N. The side force is very small and can be negligible. There is no distinct difference observed in the averaged aerodynamic forces. The small differences in the last digit can be attributed to the uncertainty of the measurement. The uncertainty of the force measurement was estimated to be within ±0.01 N. The sound pressure level (SPL) for tonal sound at fundamental frequencies (f_f) 21 Hz and 26 Hz and the peak SPL during the sound the measurement are also summarized in Table 1. The RMS sound pressure for 21 Hz sound is 104 dB with a peak SPL of 124 dB. The sound pressure level of the 26 Hz sound was adjusted by changing the power input through the sound amplifier. The RMS SPL was adjusted from 107.9 dB to 100.4 dB.

Table .3 Averaged aerodynamic forces with different sound effect

	Tonal SPL at f_f (dB)	**Peak SPL (dB)**	**Thrust (N)**	**Side force (N)**	**Lift (N)**
Without sound	--	--	0.060	0.004	0.064
21hz sound	104	124	0.060	0.003	0.062
26 Hz sound	107.9	125	0.066	0.000	0.064
26 hz sound	107.8	122	0.060	-0.001	0.063
26 hz sound	106.5	112	0.063	-0.001	0.064
26 hz sound	100.4	106	0.063	-0.005	0.066

Even though the sound effect does not appear in the averaged forces, it might be interesting to see if there is any effect on the instantaneous forces in the time history. As shown in Fig. 21, high-frequency vibrations showed in the time history of the force. A 20th order low pass FIR filter was applied to the signal to attenuate the components of the signal above 50 Hz. The filtered signal with smaller amplitude is believed to fairly present the temporal behavior of the thrust and lift generation during a complete flapping cycle, which is shown as the red curve in Fig. 21. The blue circles represent the PIV test points. Although the low filter is used, the vibration effect does not disappear, and only those very high vibration frequencies were removed from the signal. It should also be noted that the inertia effect becomes involved in the force measurements, which cannot be excluded from the current experimental setup. The phase angle within one period of the flapping was assigned from 0 to 360 degrees. The 0 phase is defined as the leading edges of the two wings clapped together completely. After this point, the two wings start to fling to the most open position at a phase angle of 180 degrees, and then clap again until totally clapped at 360 degrees. Analysis about the thrust and lift forces can be found in the previous research (Huang et al., 2013).

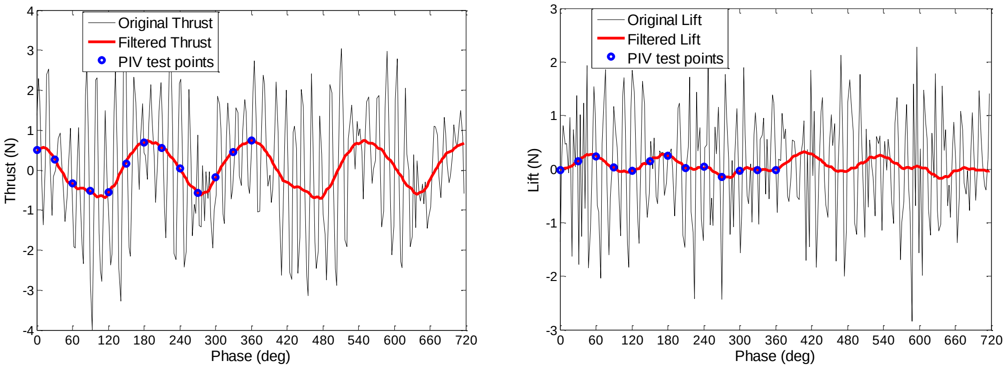

Fig. 21 Filtered Aerodynamic forces from the original time-domain signal

The comparisons of the synchronized three components of forces for the first three cases in Table 1 were presented in Fig. 22 through Fig. 24. T is the period of the flapping cycle. Fig. 22 shows the time histories of the lift for the original case, the case with 21 Hz sound effect, and 26 Hz sound effect. It is obvious that there is difference around half period and in the last 1/4 period. The one with the 21 Hz sound effect tends to have a higher absolute value of lift at these two time instants;

however, the 26 Hz sound makes the lift slightly lower at these two time instants. Similar variances were also found in the other two cycles. Actually, the differences were observed all through the measurement data that are not shown in the plot. In Fig. 22 (b), the synchronized sound pressure was also inserted into the plot to observe the coherent correlation, if any, between the sound wave and the difference in lift. It can be observed that a positive difference (i.e. increase of lift) corresponds to a negative sound pressure and vice versa. This indicates that a negative sound pressure would increase the lift of the four wing flapper under the current experimental situation. In the present experiment, the flapping frequency of the wings is about 15.2 Hz to 15.7 Hz. There are about four waveforms showing up in one period for the lift, which correspond to 60.8 Hz to 62.8 Hz, while the peak sound pressure was found at 63 Hz for the 21 Hz sound from the loudspeaker as depicted in Fig. 19 (a). This coincidence actually makes the curves shown in Fig. 22 (b) repeatable. Even though it is not exactly the same, the curves in Fig. 22 (b) are very typical and can characteristically represent the sound effect over a period. The instantaneous difference in lift is around 0.05~0.1 N. In spite of the small value, it is still considerable when taking into account the fact that the average lift is only 0.06 N. Surprisingly, the averaged lift was not influenced by the sound disturbances, which is mainly attributed to the fact that the sound wave makes both increase and decrease at some point within every single period, and the integration leads to a zero change.

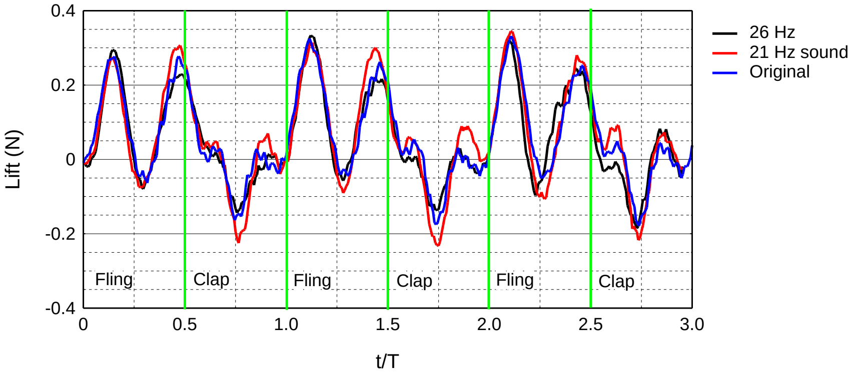

(a) Sychronized lift forces for three cases in three cycles

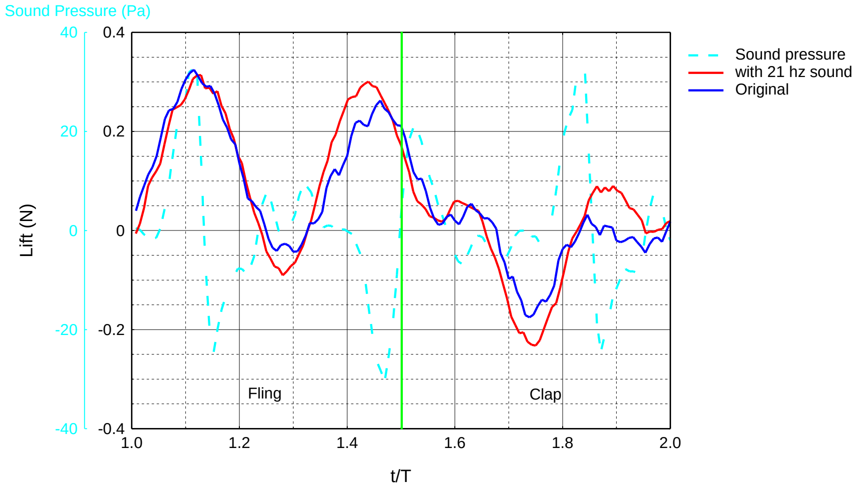

(b) Sychronized lift forces for original and 21 Hz sound cases in one cycle

Fig. 22 Effect of sound disturbances on lift at 21 Hz

Compared with the lift measurements, the thrust does not change most of the time in a period. It can be seen from Fig. 23 (a) that the thrust time histories for all three cases match with each other very well except for the time interval between around 0.2T and 0.4 T within one period. In this time interval, the two wings undergo a fling motion, which corresponds to a phase angle between 72 degrees and

144 degrees, as shown in Fig. 26. It can be estimated that the tension in the materials of the wing under these open positions maintains a relatively low level and thus the wing is more subject to sound disturbances. There are about two waveforms showing up in one period for the lift, which corresponds to 30.4 Hz to 31.4 Hz. Therefore, the sound wave at 63 Hz is still approximately a harmonic wave to the thrust wave. The difference generated by the sound effect on lift could be approximately 0.05 N∼ 0.1N in the time interval between 0.2T and 0.4T. Again, the increase balances with the decrease in a whole period; therefore, there is no observable difference for the averaged thrusts in Table 1.

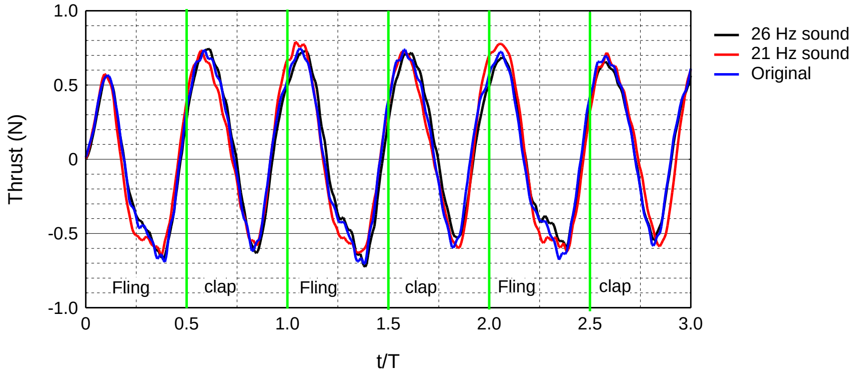

(a) Sychronized thrust forces for three cases in three cycles

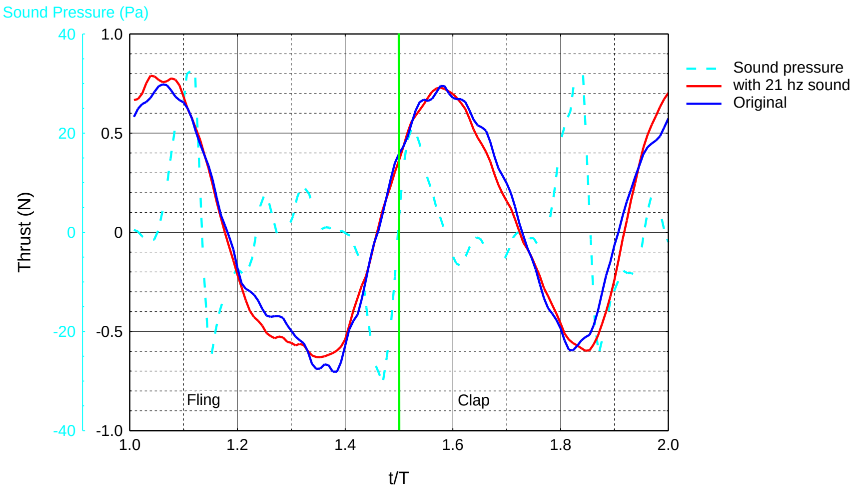

(b) Sychronized thrust for original and 21 Hz sound cases in one cycle

Fig. 23 Effect of sound pressure on thrust at 21 Hz

Since the sound source was positioned in the side of the flapper, the most significant effect was expected in the measurement of the side force. As shown in Fig. 24, both 21 Hz and 26 Hz have significant effects on the side force, while the 21 Hz sound induces more variations. The maximum change of the amplitude can reach around 0.25 N. The waveforms of the three cases in the first half of each cycle match with each other very well; however, the waveform shapes in the second half do not match well. It should be noticed that the sound frequencies, both 21 Hz and 63 Hz, are not coincident with the frequency of the side force (around 90 Hz). Therefore, the results shown in Fig. 24 (a) and (b) do not repeat in other cycles very well. Fig. 24 (b) shows the side forces for the case without sound disturbances and the with 21 Hz sound with sound pressure history inserted. The inversed correlations between the variation of side force and sound pressure appear again, although it is not rigorous over the whole period. It should be noted that the direction of the positive pressure corresponds to the negative direction of the side force in the present experimental setup.

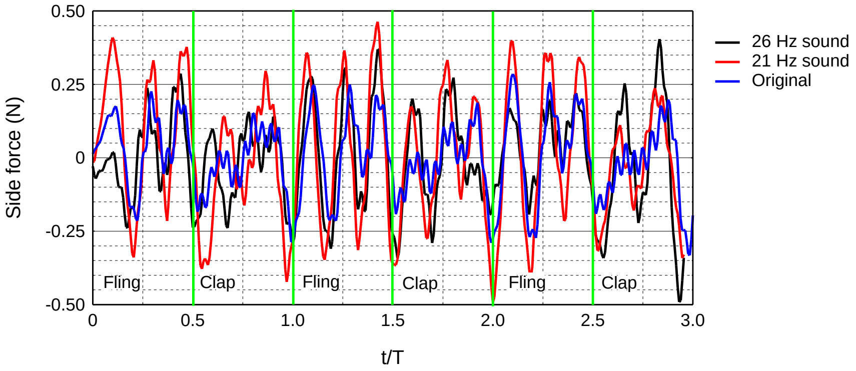

(a) Sychronized side forces for three cases in three cycles

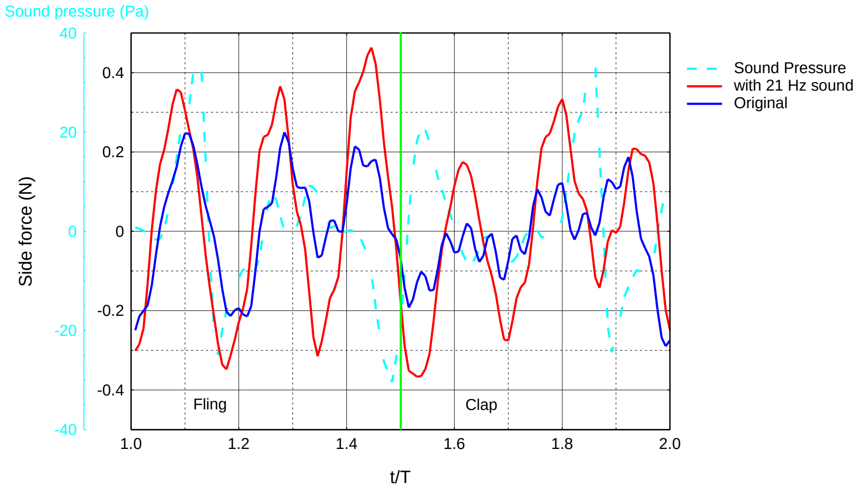

(a) Sychronized side forces for original and 21 Hz sound cases in one cycle

Fig. 24 Effect of sound pressure on side force at 21 Hz

The effect of amplitude of the sound disturbances was also studied in the present study. The frequency of the sine signal generated by the function generator was fixed at 26 Hz. The amplitude of the sound wave was adjusted from 108 dB to 100 dB by varying the gain value of the amplifier. Surprisingly, the same frequency sound with lower amplitude tends to have more influence on the lift and side forces, which can be clearly seen in Fig. 25 (a) and (b). Compared with the 26 Hz sound at 108 dB, the 26 hz sound at 100 dB results in a more distinct difference in both instantaneous lift and side forces. As shown in Fig. 19, with the decrease of the gain value of the amplifer, the low frequency sound wave becomes more dominant in the amplitude spectrum. The change of the dominant frequency in the sound is believed to cause the difference of the sound effect on lift and side forces. It also indicates that the lower frequency at 26 Hz could induce significant change in lift and side forces, but this effect can be restricted by its higer order harmonics with considerable amplitudes.

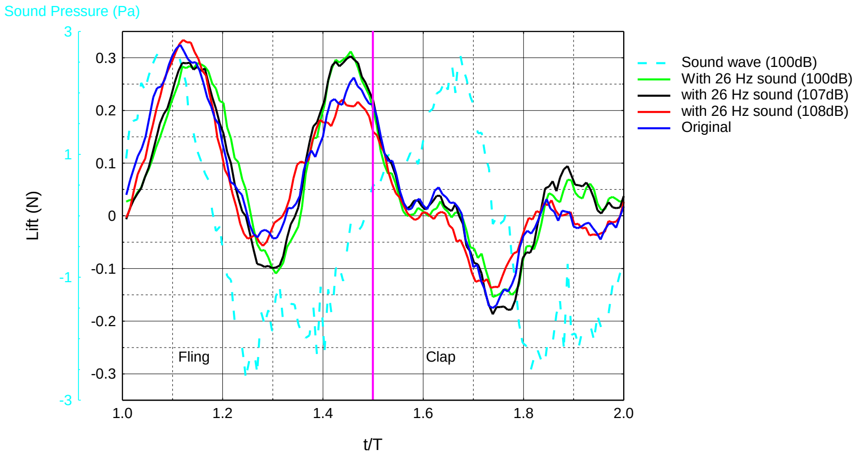

(a) Effect of sound pressure on lift

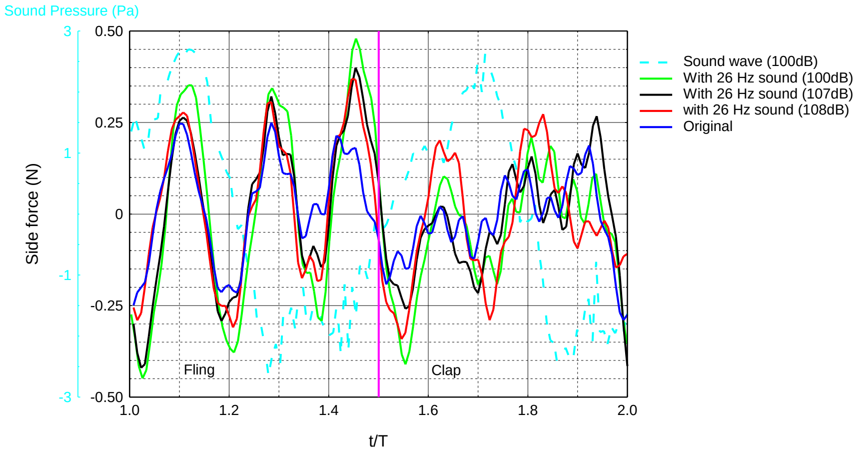

(b) Effect of sound pressure on side force

Fig. 25 Effect of sound pressure on the aerodynamic forces at 26 Hz

4.4 Effect of acoustic disturbances on flow field around flapping wings

Fig. 26 shows the detailed flow field measurements around two flapping wings in one side, with and without acoustic disturbances. The wings shown in the PIV measurement are the left hand side wings when facing the flapper head. Only the PIV measurements in the vertical plane crossing the middle position in spanwise were presented in the paper. Fig. 26 (a) and (b) shows the averaged phase-lock PIV measurement result when the wings are clapping together (known as “clap”). Fig. 26 (i) and (j) show the averaged phase-lock PIV measurement result when the wings are expanding to the maximum angle (known as “fling”). The most import region has been circled in each plot for better comparison. The two-dimensional view of the wing shape was also extracted from the PIV measurement. Although it is not a quantitative measurement of the three-dimensional wing morphology data, it still provides qualitative wing deformation under sound disturbances to some extent. When the wings start to fling to the open position, the leading edge strut rotates fast with the gear, but other parts of the flexible wing cannot follow instantaneously. The inertial effect and the aerodynamic forces will make the wing bend to overcome the suddenly changed wing position. Some obvious differences on the wing deformation were observed at several phase angles. At phase angles of 90 degrees, 120 degrees and 150 degrees, the inside wing bent more without sound disturbances, which can be seen from the curvature of the trim of the inside wing. This implies that the sound disturbances straighten out the wing at these positions.

The sound effect does not show up in the flow field at the phase angle of 0 degrees. But from 90 degrees, the sound influence on the flow field is observable. The sound disturbances slow down the flow velocity right after the wing, but the flow structure (i.e vortex structure) does not change. At the phase angle of 120 degrees, the flow velocity is intensified, and the flow structure changes drastically. The wake flow turns down quickly with the sound disturbances. And this trend attenuates gradually to the phase angle of 150 degrees. The increase of the downward velocity might lead to an expectation of an increase of the lift. This expectation agrees fairly well with the fact of the instantaneous lift measurements, as shown in Fig. 22. After the totally open position, from a phase angle of 180 degrees to 270 degrees, the change in the flow field is a little hard to observe.

Actually the flow with sound effect in the region below the center of the circle has a little bigger component in the vertical direction compared with the flow without sound effect, although the sound effect on the aerodynamic forces is much more noticeable.

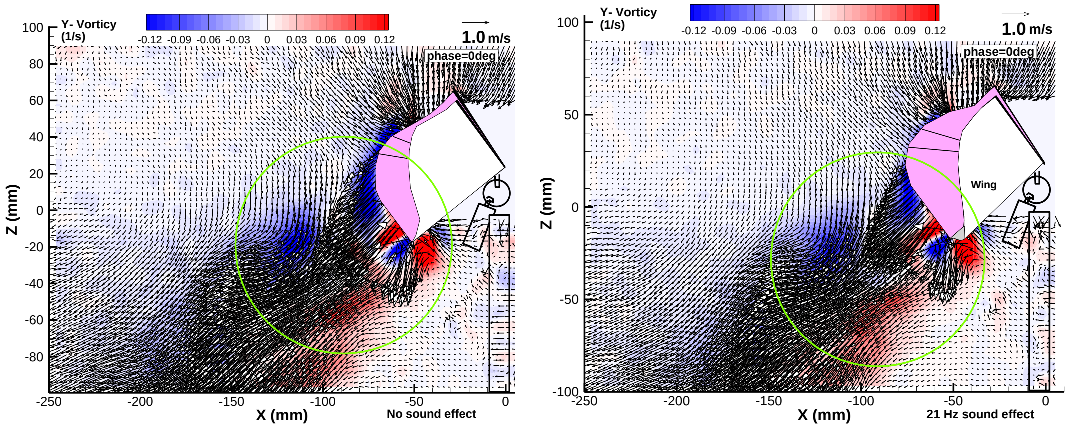

(a) Flow field without sound effect at phase=0 deg (b) Flow field with 21 Hz sound effect at phase=0 deg

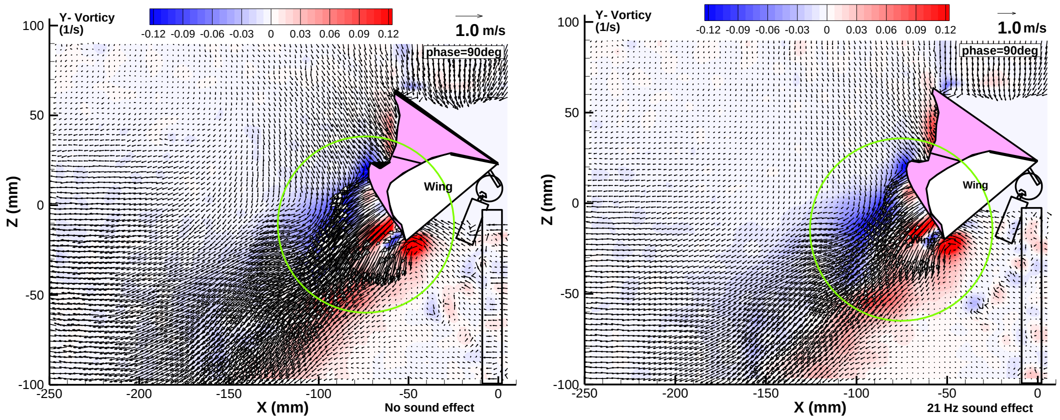

(c) Flow field without sound effect at phase=90 deg (d) Flow field with 21 Hz sound effect at phase=90 deg

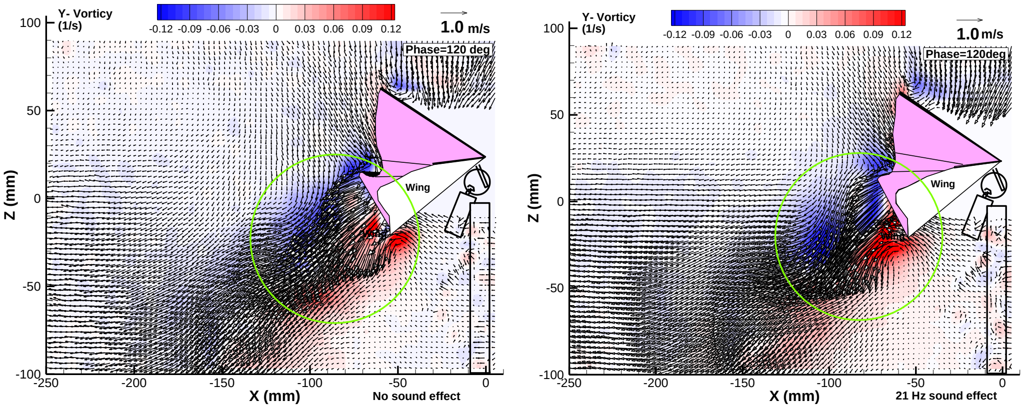

(e) Flow field without sound effect at phase=120 deg (f) Flow field with 21 Hz sound effect at phase=120 deg

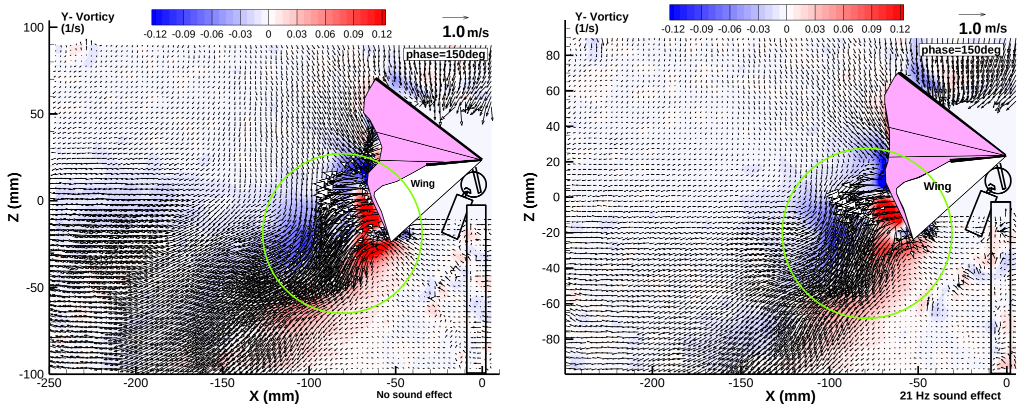

(g) Flow field without sound effect at phase=150 deg (h) Flow field with 21 Hz sound effect at phase=150 deg

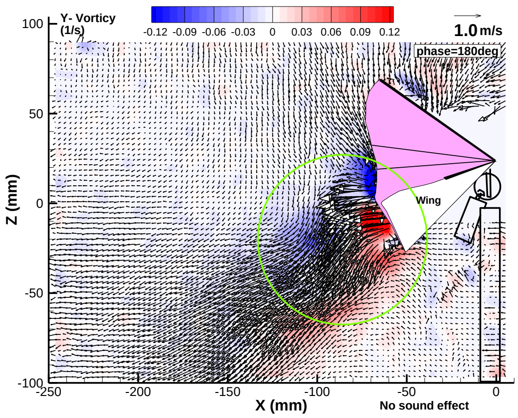

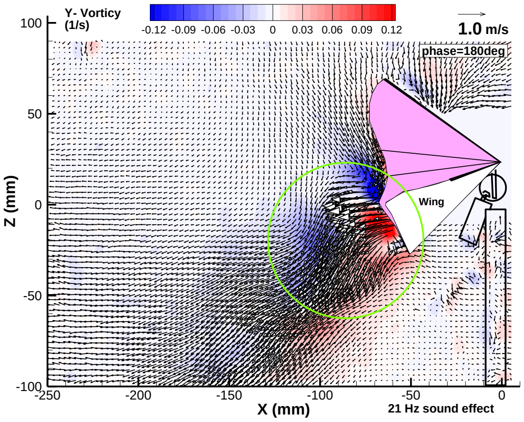

(i) Flow field without sound effect at phase=180 deg

(j) Flow field with 21 Hz sound effect at phase=180 deg

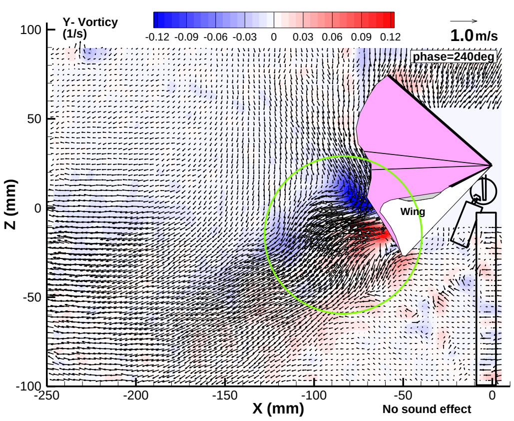

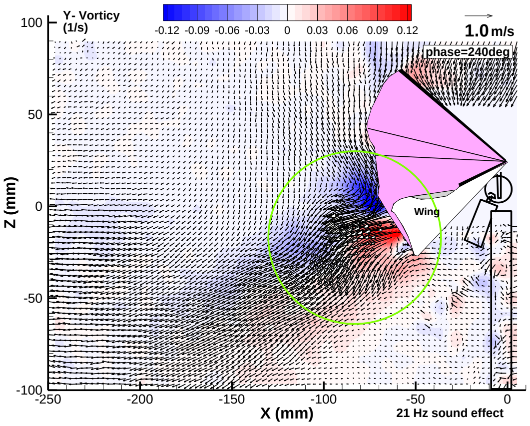

(k) Flow field without sound effect at phase=240 deg

(l) Flow field with 21 Hz sound effect at phase=240 deg

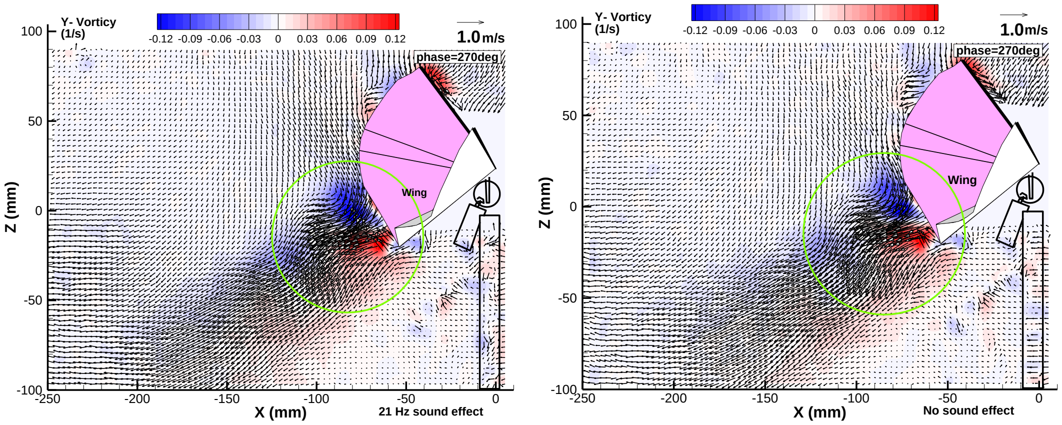

(m) Flow field without sound effect at phase=270 deg (n) Flow field with 21 Hz sound effect at phase=270 deg

Fig. 26 PIV measurements around flapping wings without and with sound disturbances at different phase angles

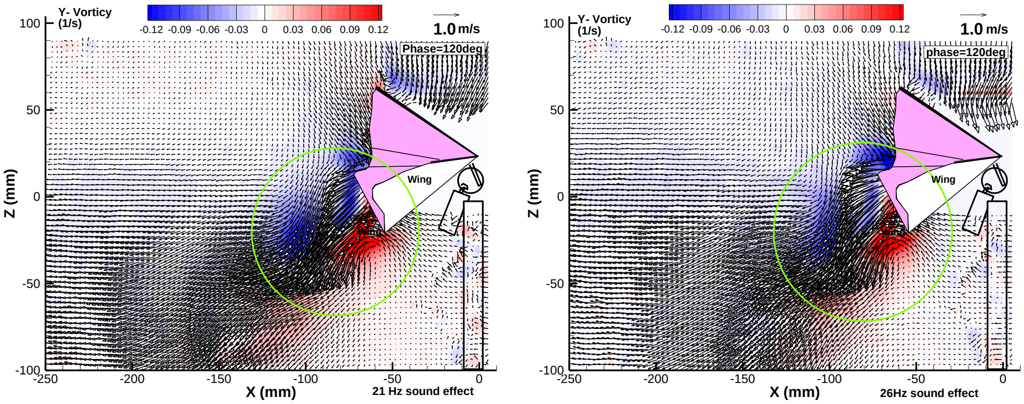

(a) Flow with 21 Hz sound effect at phase = 120deg (b) Flow with 26 Hz sound effect at phase = 120deg

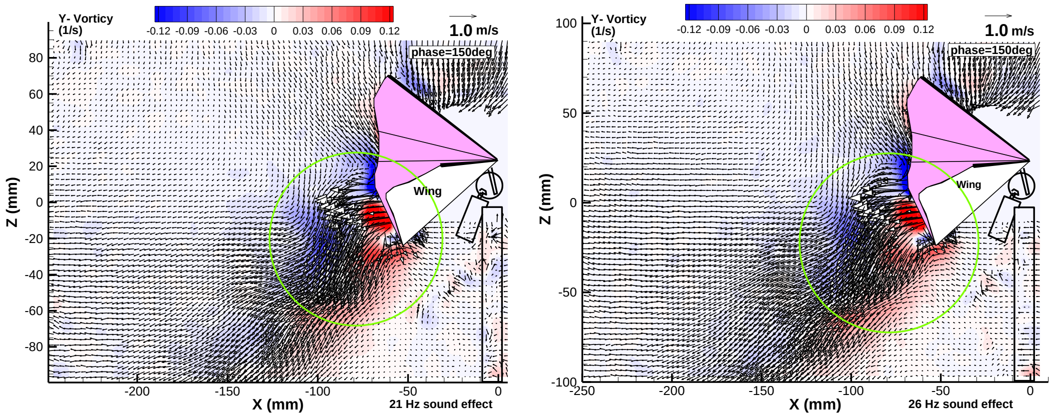

(c) Flow with 21 Hz sound effect at phase = 150deg (d) Flow with 26 Hz sound effect at phase = 150deg

Fig. 27 PIV measurements around flapping wings with 21 Hz and 26 Hz sound disturbances at different phase angles

Fig. 27 shows the PIV measurement results with sound disturbances at different frequencies. Comparing the flow at the phase angle of 120 degrees and 150 degrees, the coherent flow structure is very similar. Through a careful comparison of the flow, one may observe that the vorticity value in the region left to the center in the circle for the 21 Hz sound is higher than that for the 26 Hz sound, which implies the coherent flow structure change and velocity change. But the difference is less distinguishable compared with the differences in force measurement results. One reason for this is that the PIV measurements shown in the paper are only a 2-D flow field in one cross plane, which is not enough to map the whole flow field around the wings. Mostly, the flow field measurement can be correlated with the analysis of the force measurement results. Further experimental investigations will be conducted to characterize the 3-D flow structure change under sound disturbances. And the complicated wing deformation under sound effect needs to be quantified in order to resolve the flow structure change.

4.5 Conclusion

An experimental study was conducted to investigate the sound disturbances on the aerodynamic forces and flow around the flapping wings of a four-wing flapper. In the present study, a clap-and-fling type of four-wing flapper was designed and manufactured by using the flexible material PET film. In addition to the lift, thrust, and side force measurements using a highly sensitive force moment sensor unit, a high-resolution phase-locked Particle Image Velocimetry (PIV) system was employed to achieve detailed flow field measurements to quantify the evolution of the unsteady vortex flow structure around and/or in the downstream of the flapping wings. At the same time, the sound pressure was monitored during the experiment. During the test, all measurements were synchronized through a digital delay generator. This synchronization enables the analysis on the instantaneous correlation among the aerodynamic forces, the sound pressure, and flow field measurements.

Through the comparison of the instantaneous aerodynamic forces in correlation with the flow field information, it has been found that the sound disturbances can have considerable effects on the instantaneous force generation, especially on the lift and side forces. However, the sound effect on averaged aerodynamic forces was not observed. The most distinguishable effect was obtained on side forces with sound disturbances at 21 Hz, while several high-order harmonics were also included in the sound. In a complete cycle of the flapping, the sound disturbances have considerable effect on all three components of the aerodynamic force between approximately 0.2 T and 0.4 T (i.e. phase angle of 72 degrees to 144 degrees), which agrees with the flow filed measurements. The lift was also influenced in the last quarter of the period, while the side force was greatly affected in the whole period. The approximate inversed correlation between the sound pressure and the lift as well as the side force was observed, which means the positive sound pressure will induce a decrease of the forces, and the negative pressure will induce an increase of the forces. Last but not the least, the effect of the sound levels at 26 Hz on the lift and side forces were studied. Surprisingly, the same frequency sound with lower amplitude tends to have more influence on the lift and side forces, which is due to the fact that with the decrease of the gain value of the amplifer, the low frequency sound wave becomes more dominant in the amplitude spectrum. It is believed that the change of the dominant frequency causes the increase of the sound effect on lift and side forces.

5. Wing Deformation and Stereo-PIV Measurements

5.1 Digital Image Correlation

Digital Image Correlation (DIC) in an optical method to measure deformation on an object surface. The method tracks the grey (intensity) value pattern in small neighborhoods called windows during deformation, as shown in **Fig. 28**. A single camera can be used to measure the deformation in a 2-D plane. Two cameras can be used to measure the deformation in three dimensions using appropriate stereo-correlation as shown in **Fig. 29**. **Fig. 31 through Fig. 35** show the results of the flexible-wing deformation at a phase angle of 150 degrees (close to wide open position) using the DIC technique. The DIC technique was widely applied in the field of material testing including Young's Modulus, Poisson's ratio, dynamic measurements, and displacement measurements. In the present research, as the deformation for the proposed research is relatively large and the range of the flapping motion is also wide (approximately 0 – 120 degree) as shown in **Fig. 35**, many difficulties arise when conducting the experiment. Several perspective angles are needed for installing the cameras if one wants to observe the deformation of two wings during the whole flapping cycle. In order to accurately measure the deformation at different phase angles (angle position of the flapping wings), the phase-lock technique will be applied to the DIC measurements by using appropriate digital delay generators.

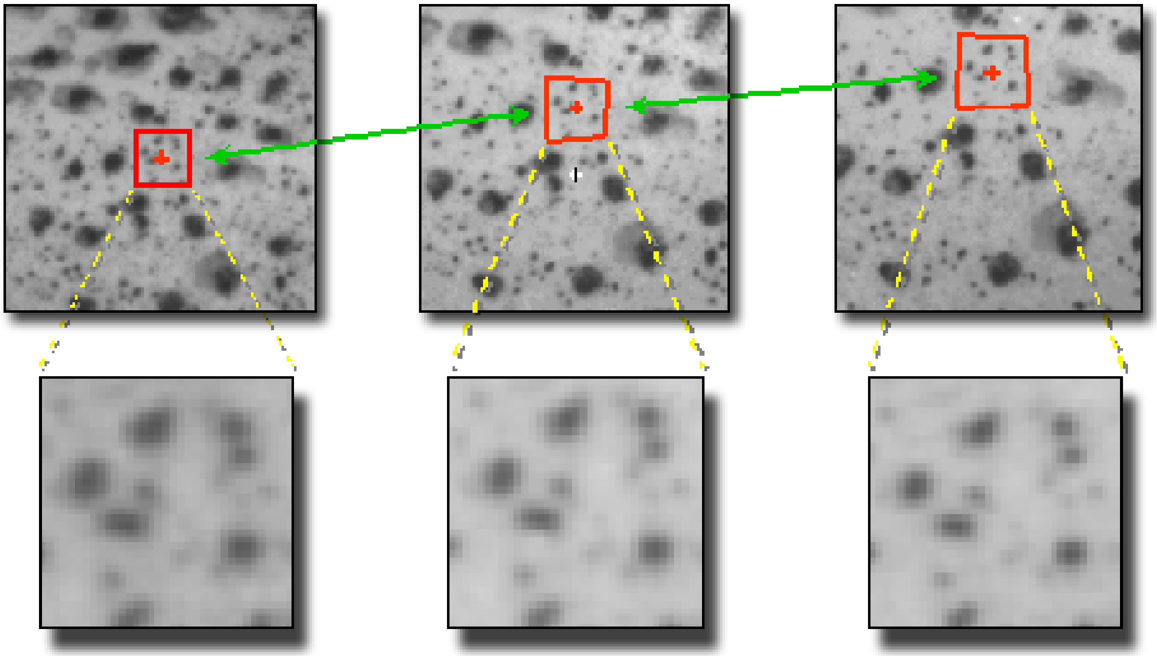

Time t Time t' Time t"

Fig. 28: Images at different time instance for DIC

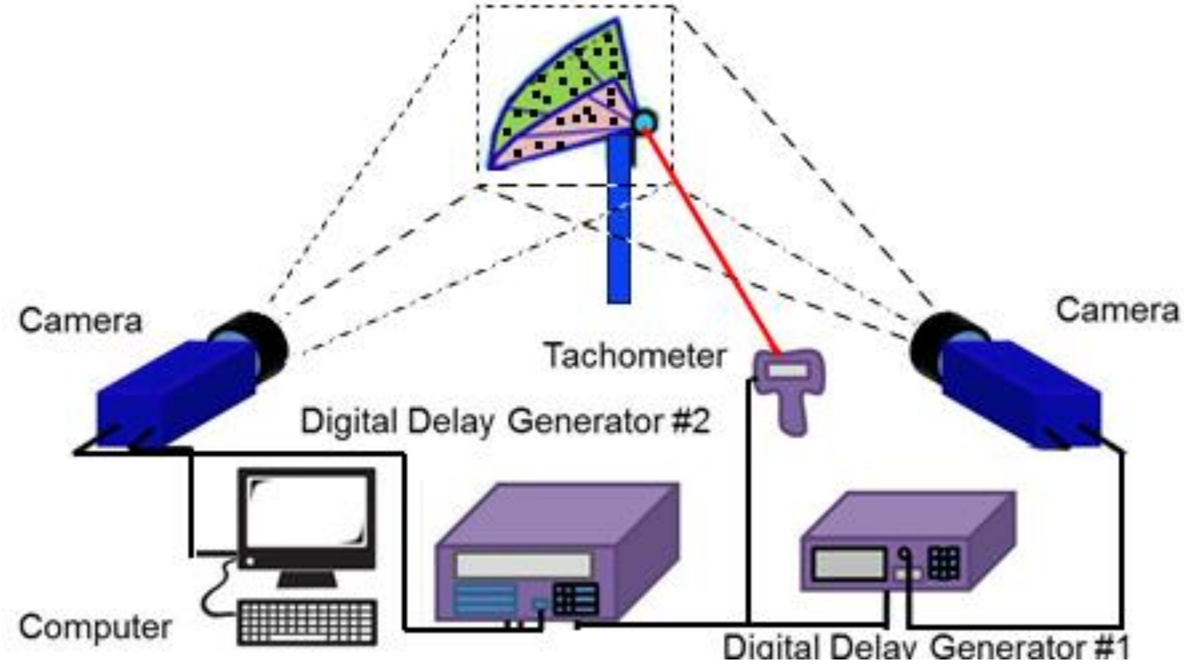

Fig. 29: Schematic of experimental setup for DIC

The study on the deformation measurements of the wings in the wind tunnel was conducted recently in the Ohio Center for Micro Air Vehicle Studies (CMAVS) in the Department of Mechanical and Materials Engineering at Wright State University. **Fig. 29** shows the experimental setup, which includes two digital cameras and three light sources with the flapping-wing flyer model installed in the test section of a low-speed wind tunnel. An in-house C++ code has been developed to correct the edge and filter the measurement noise in the data. **Fig. 30** presents the calibration image and raw images captured using the DIC system. **Fig. 31 through 35** present the post-processed data for the wings' geometry and position in the 3-D and 2-D coordinate system.

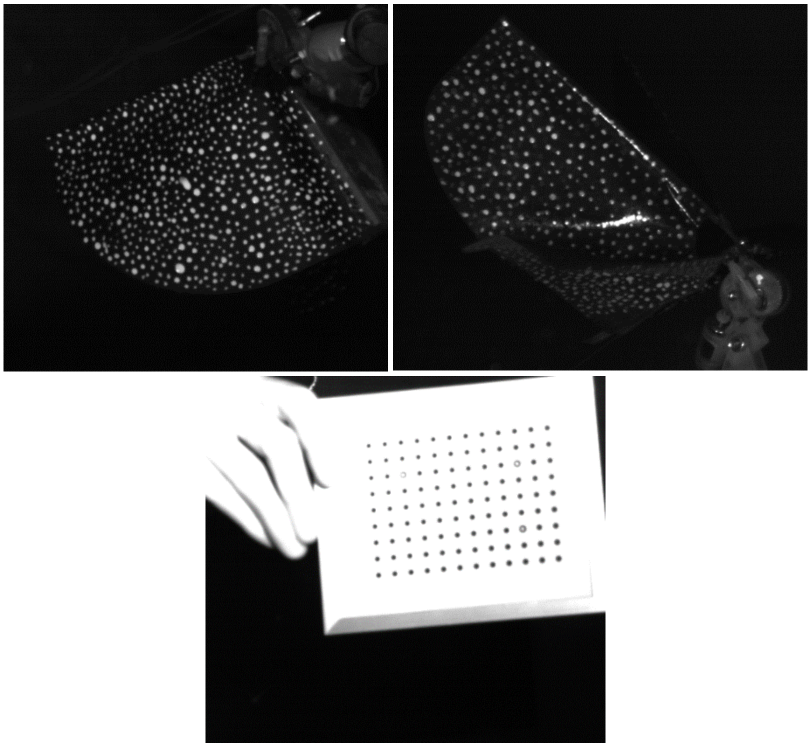

(a) **(b)** **(c)**

Fig. 30: DIC images: (a) calibration image (b) bottom view (c) side view

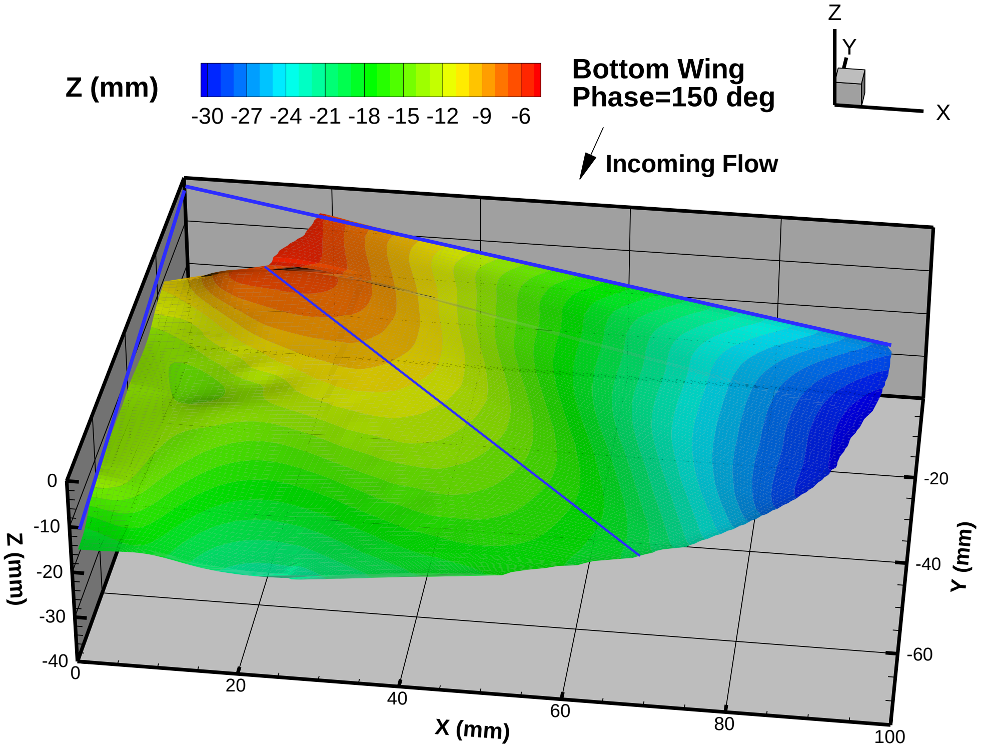

Fig. 31: Bottom wing deformation at phase angle of 150 degree

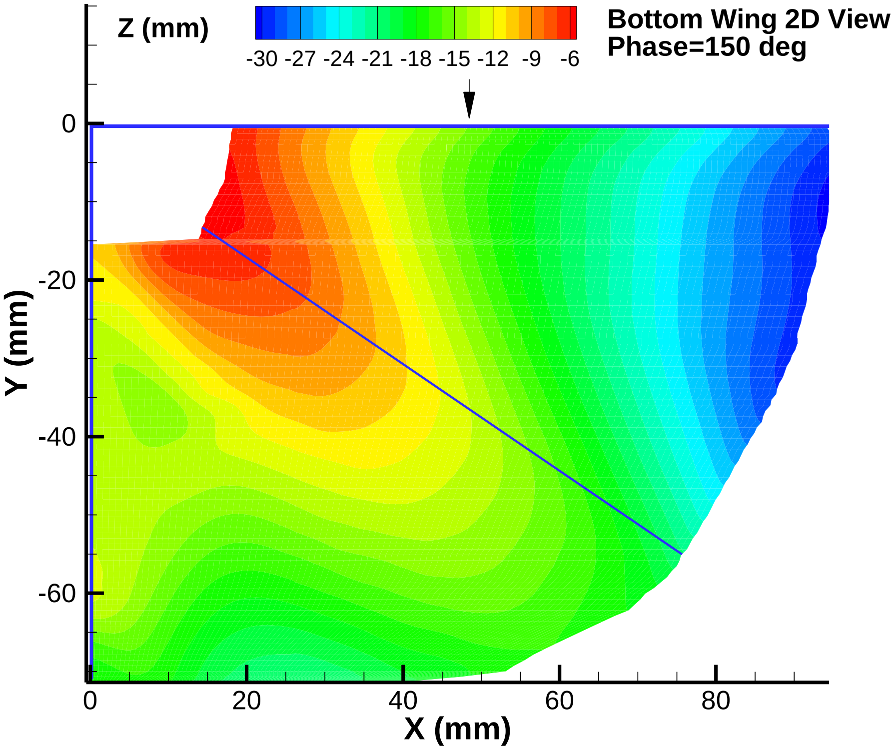

Fig. 32: 2D view of the bottom wing deformation at phase angle of 150 degree

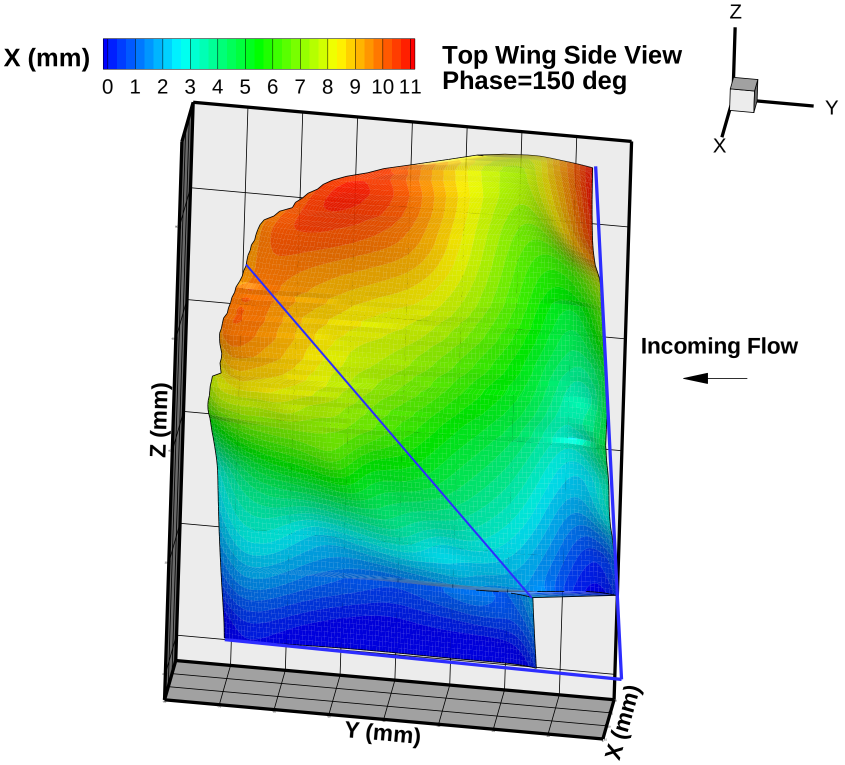

Fig. 33: Top wing deformation at phase angle of 150 degree

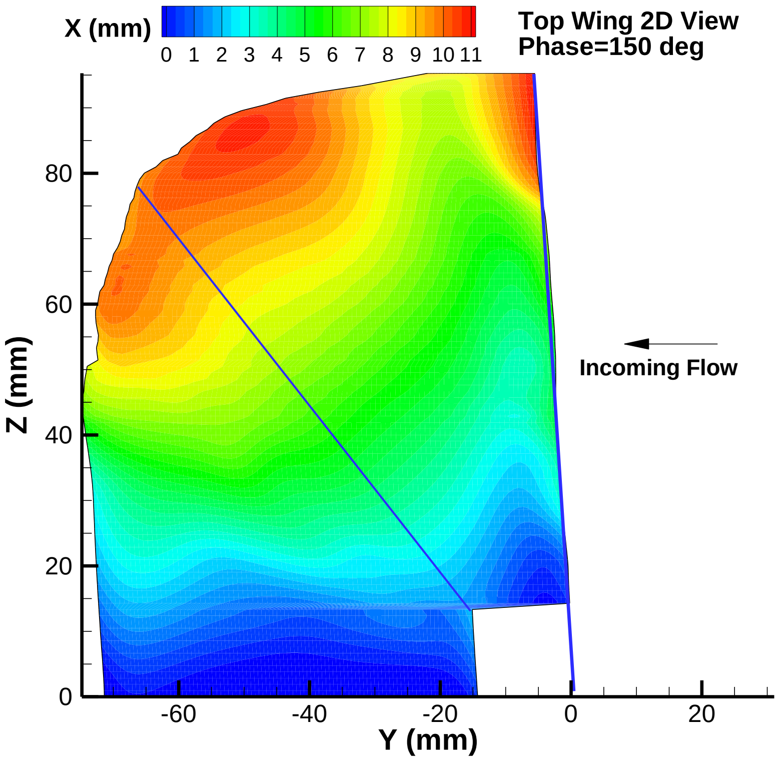

Fig. 34: 2D view of top wing deformation at phase angle of 150 degree

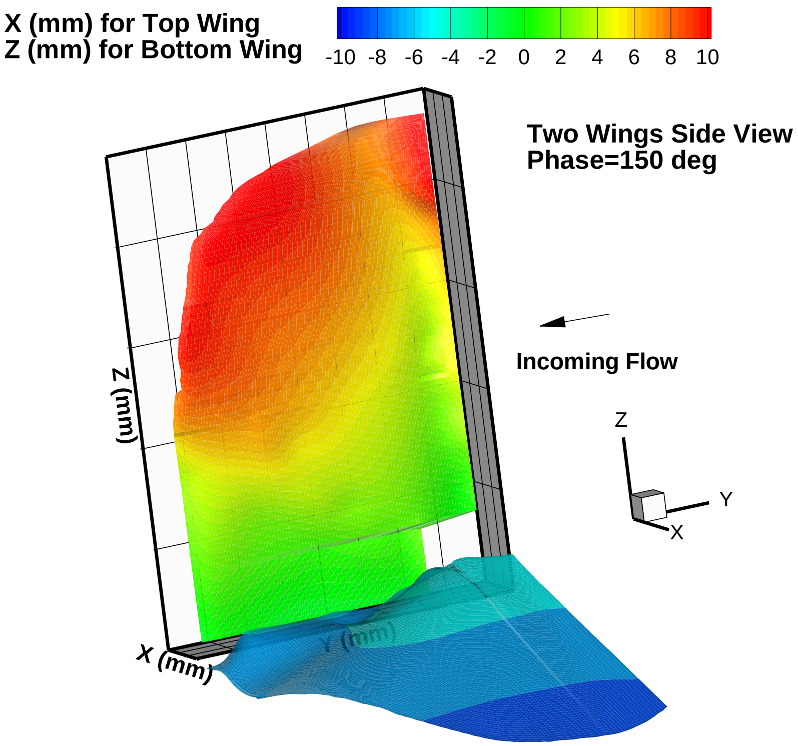
X (mm) for Top Wing
Z (mm) for Bottom Wing
-10
-8
-6
-4
-2
0
2
4
6
8
10
Two Wings Side View
Phase=150 deg
Incoming Flow
Z
Y
X
Z (mm)
X (mm)
Y (mm)

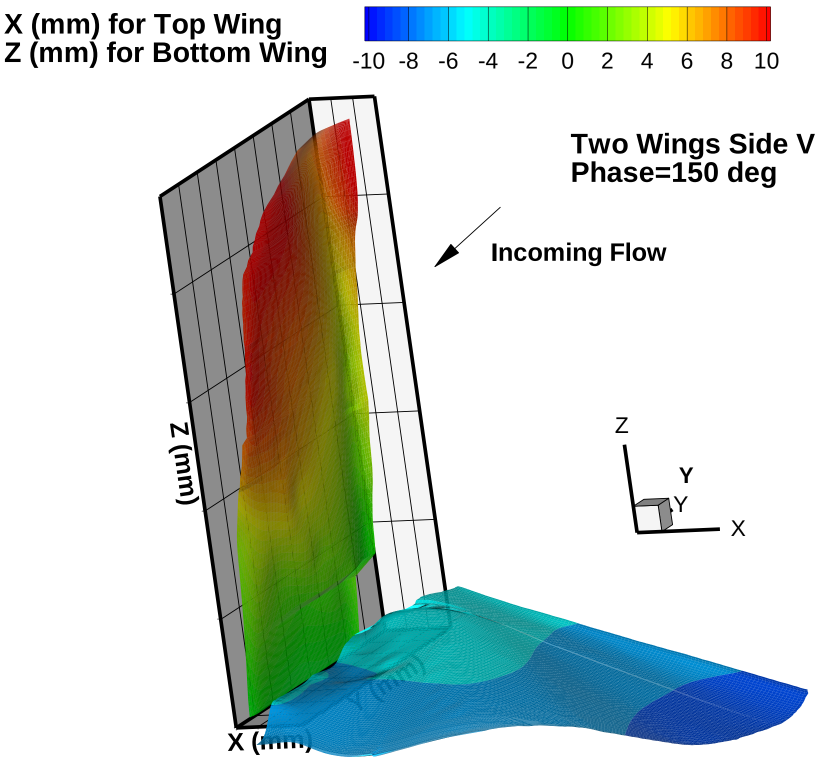

Fig. 35: Side view of combination of two wings at phase angle of 150 degree from different perspective angle

5.2 Stereo PIV

A conventional 2-D PIV system is only capable of obtaining two components of velocity vectors in the plane of the illuminating laser sheet. The out-of-plane velocity component is lost, while the in-plane components may be affected by an unrecoverable error due to perspective transformation. As shown in **Fig. 36**, a Stereoscopic PIV system (SPIV) utilizes two cameras, simultaneously viewing the same region from different perspectives. The projections of flow velocity vectors on the two image planes of the cameras can be combined to reconstruct all three components of the velocity vectors. By scanning the illuminating laser sheet through the region of interest, whole-field measurements of all three components of flow velocity vectors in a three-dimensional space can be obtained.

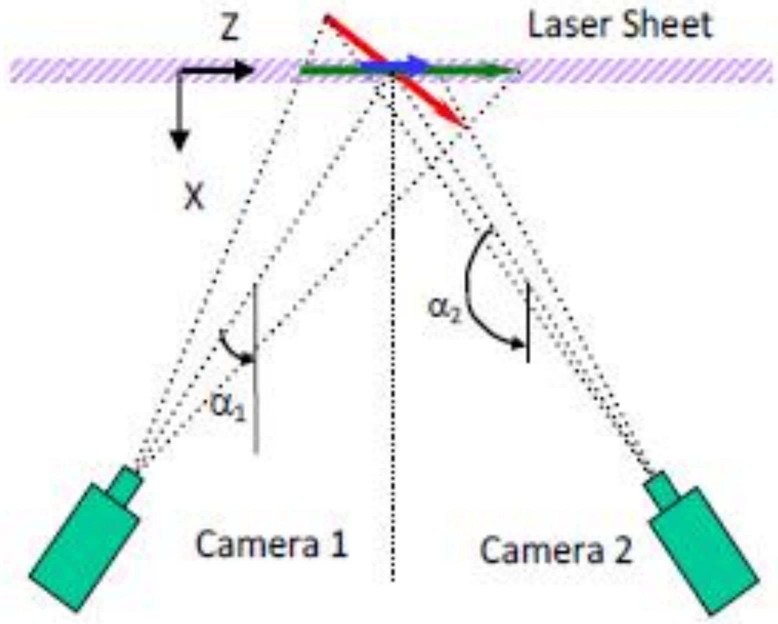

Fig 36: Schematic of stereo image technique

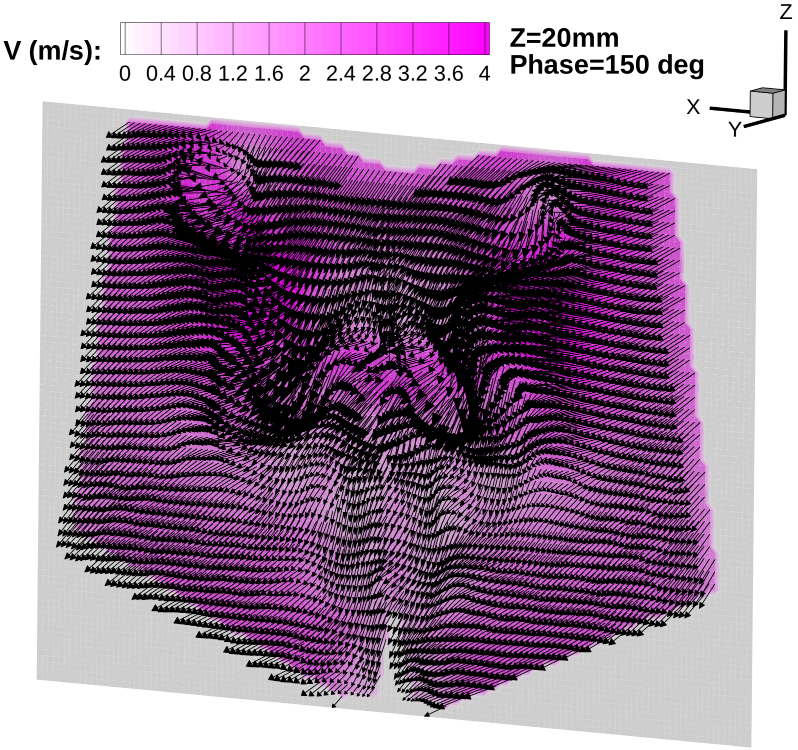

(a) Stereo PIV velocity vectors

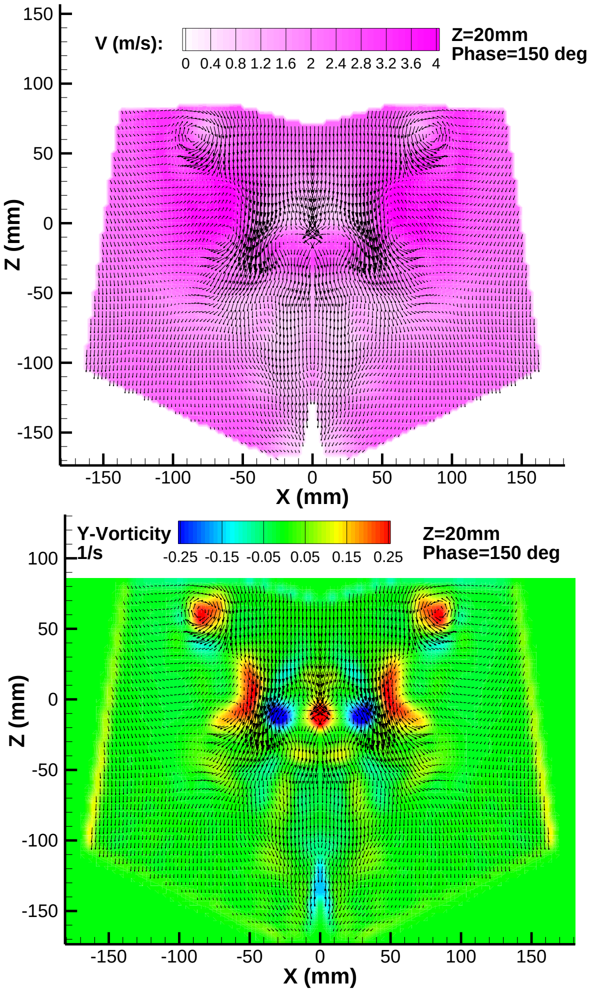

(b) 2-D vectors in the measurement plane

(c) Y-direction Vorticity distribution

Fig 37: Stereo PIV measurements on the plane at y = 20mm away from the trailing edge of the flapping wing MAV at phase of 150 degree

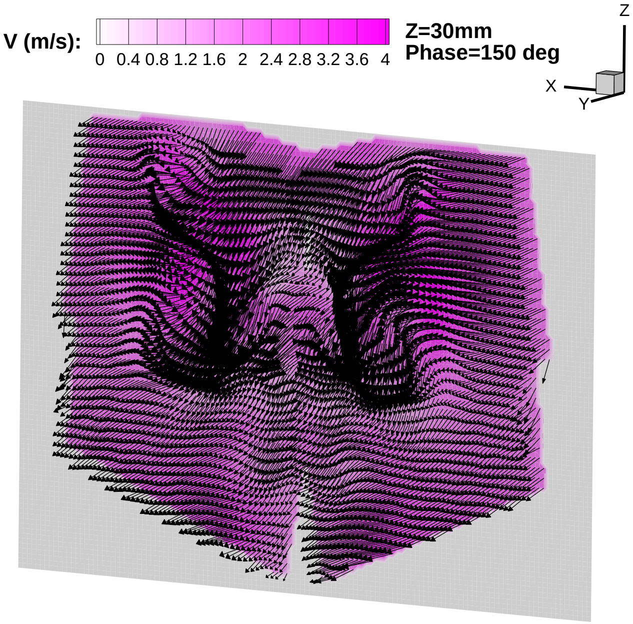

(a) Stereo PIV velocity vectors

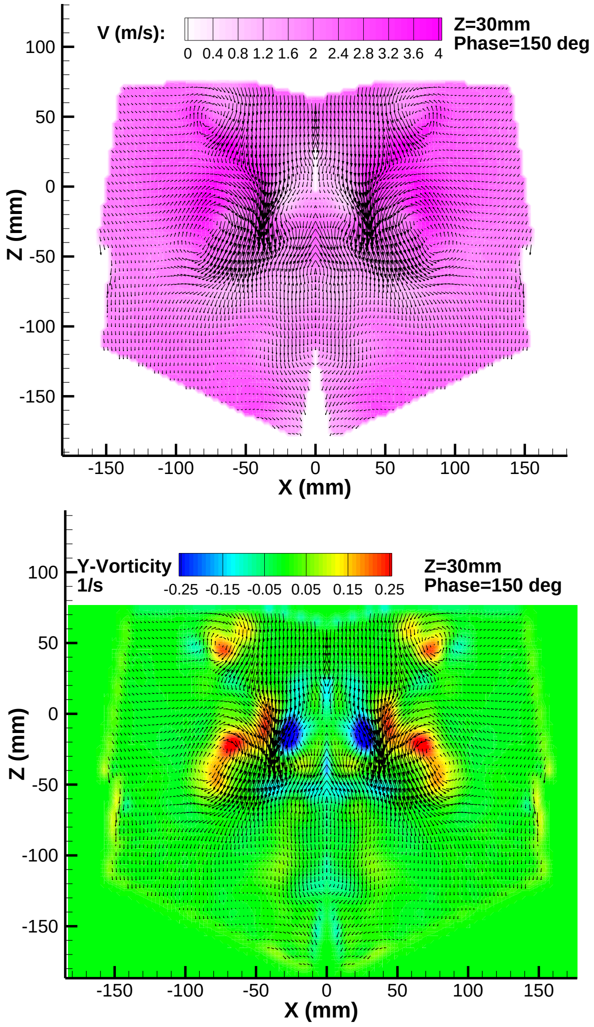

(b) 2-D vectors in the measurement plane (c) Y-direction Vorticity distribution

Fig 38: Stereo PIV measurements on the plane at y = 30mm away from the trailing edge of the flapping wing MAV at phase of 150 degree

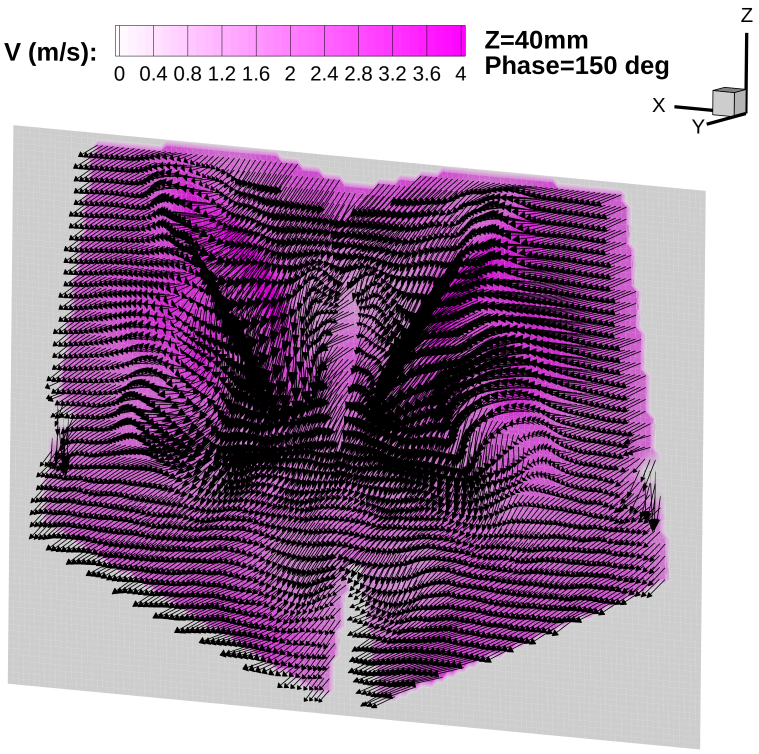

(a) Stereo PIV velocity vectors

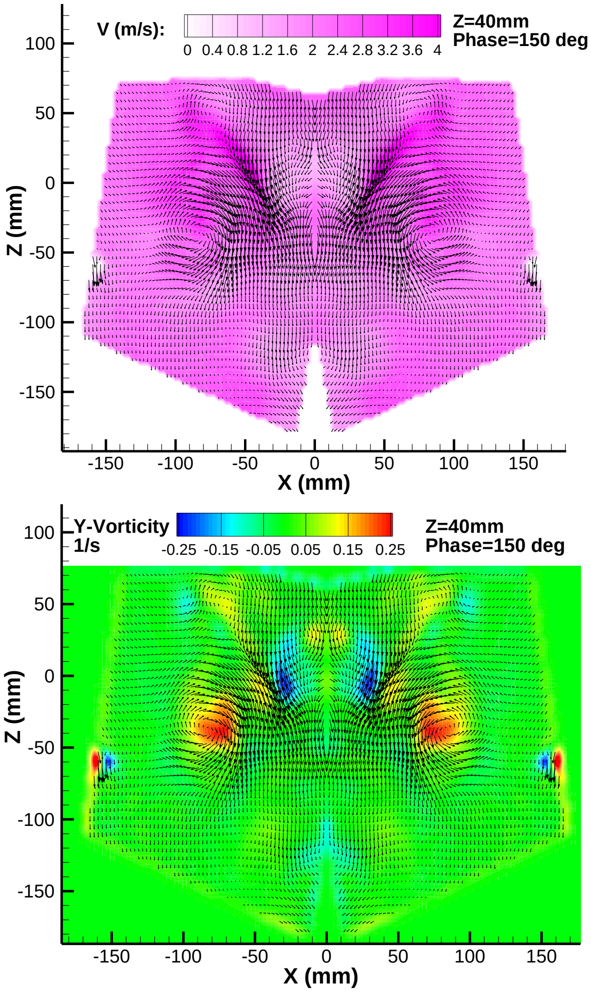

(b) 2-D vectors in the measurement plane (c) Y-direction Vorticity distribution

Fig 39: Stereo PIV measurements on the plane at y = 40mm away from the trailing edge of the flapping wing MAV, at phase of 150 degree

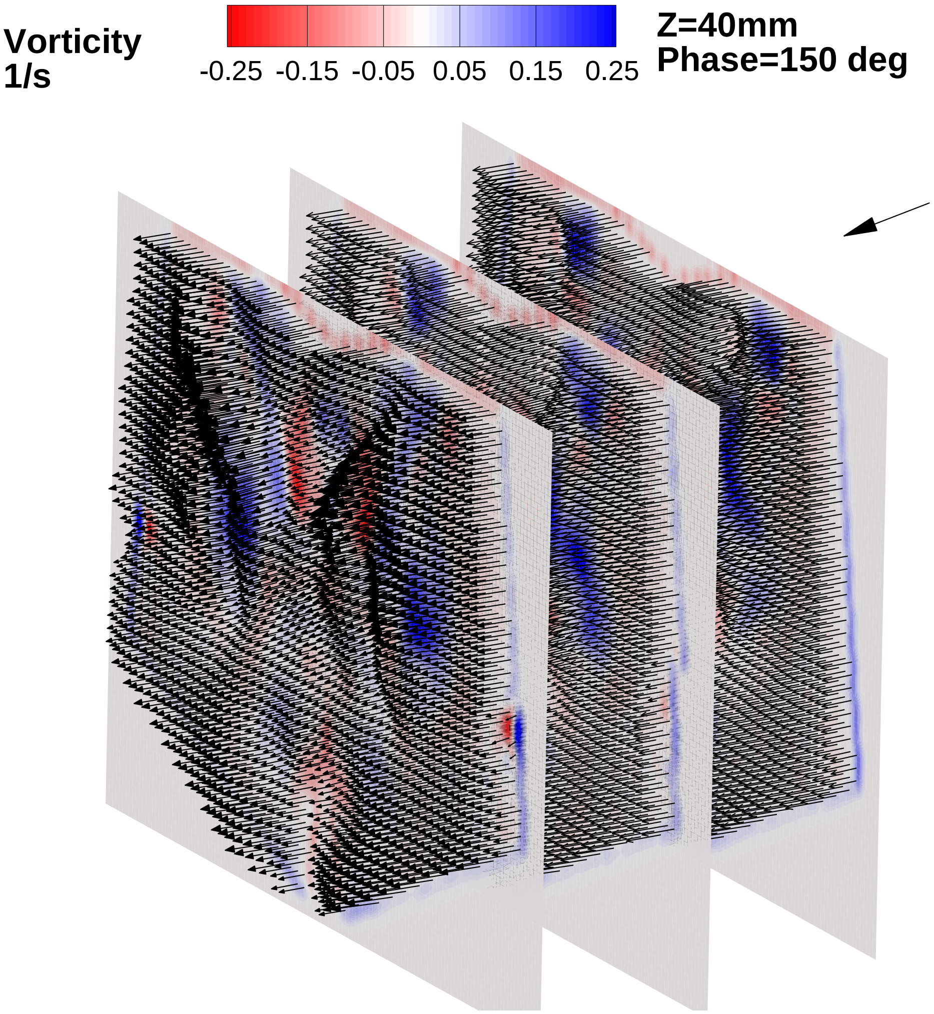

Fig 40: The combination of the three Stereo PIV measurements planes

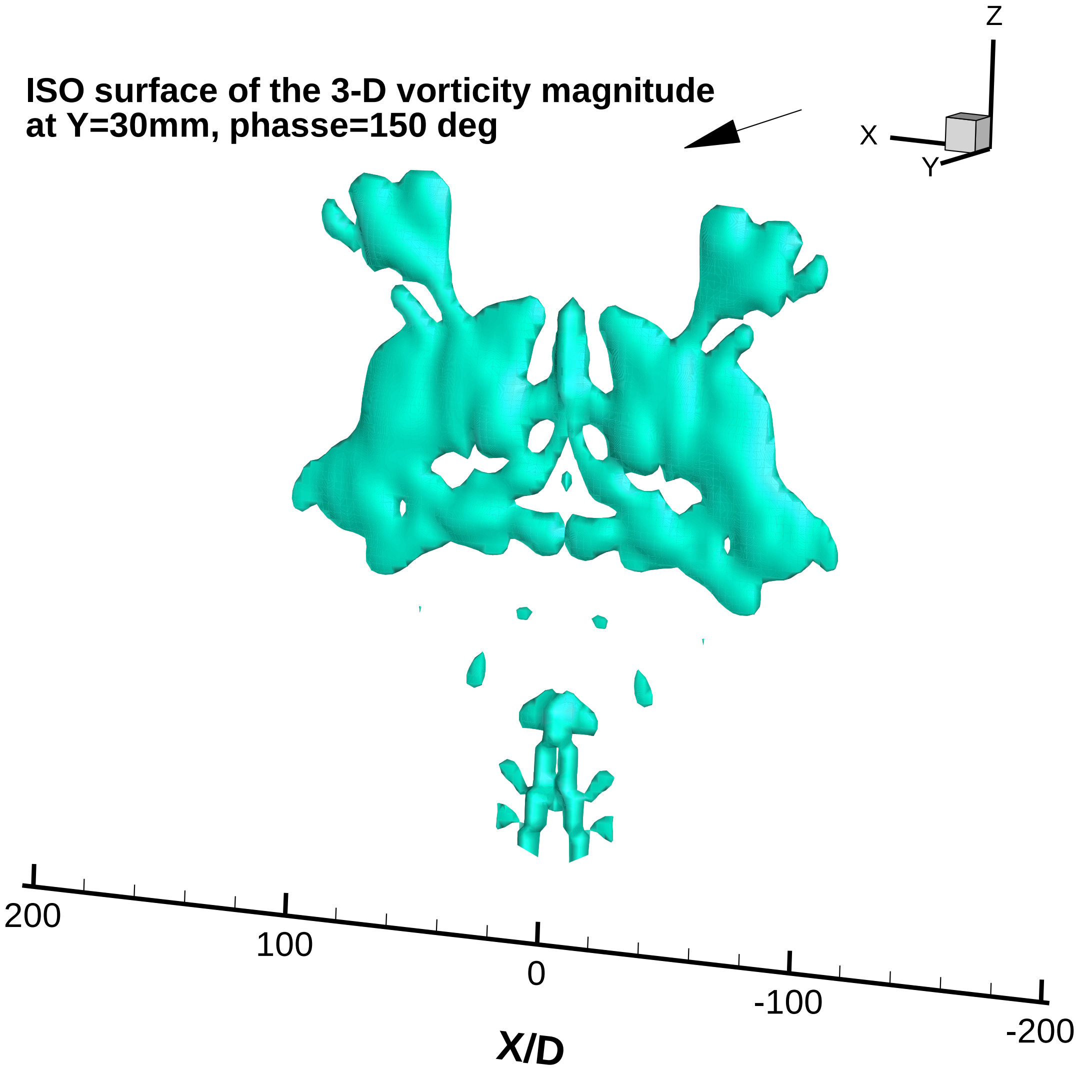

Fig 41: 3D ISO surface of the vorticity magnitude (ω=0.25)

5.3. Conclusion

An experimental study was conducted to investigate the flow field of the four-wing flapper. The lift and thrust coefficient of a four-wing flapper is also conducted. The result shows that the Cross strut pattern affects both the force measurement and flow structure. The result has been found that the sound disturbances can have considerable effect on the instantaneous force generation, especially on the lift and side forces. However, the sound effect on averaged aerodynamic forces was not observed. The most distinguishable effect was obtained on side forces with sound disturbances at 21 Hz while several high-order harmonics were also included in the sound. In a complete cycle of the flapping, the sound disturbances have considerable effect on all three components of the aerodynamic force between approximately 0.2 T and 0.4 T (i.e. phase angle of 72 degree to 144 degree), which agrees with the flow filed measurements. It is believed that the change of the dominant frequency causes the increase of the sound effect on lift and side forces. Stero PIV and DIC is being appplied to measure the 3D flow structure and wing deformation of a four-wing flapper, and future study will be needed.

Nomenclature

AOA = angle of attack

c = chord length of the wing

CL = lift coefficient

CT = thrust coefficient

g = acceleration of gravity

m = mass of the wing

s = span of the wing

Fx = force acting on the four wing flapper in x direction

Fy = force acting on the four wing flapper in y direction

Fz = force acting on the four wing flapper in z direction

RTW = the ratio of thrust to weight

S1 = cross strut pattern one

S2 = cross strut pattern two

S3 = cross strut pattern three

x = axial coordinate

y = vertical coordinate

z = transverse coordinate

ρ = air density

$U\infty$ = mean velocity of the uniform flow

References

1. *Ahuja, K. K., Whipkey, R. R., and Jones, G. S. (1983) Control of turbulent boundary layer flows by sound, AIAA 8th Aeroacoustics Conference, AIAA Paper 1983-0726.*
2. *Baker T.C., and Carde, R.T. (1978) Disruption of gypsy moth male sex pheromone behavior by high frequency sound, Environmental Entomology, Vol. 7, pp.45-52.*
3. *Ffowcs Williams, J.E. (1984) Anti-Sound, Proceedings of the Royal Society of London, Series A, 395(1808): 63-88.*
4. *Hakan H. A., Serdar M. G., Tugrul, M. A. and Karasu, I. (2012) An experimental study of acoustic disturbances effect on laminar separation bubble and transition over an aerofoil at low Reynolds number, AIAA 2012-2684, 6th AIAA Flow Control Conference, New Orleans, Louisana.*
5. *Ho, S., Nassel, H., Pornsinsirirak, N., Tai, Y., Ho, C. (2003) Unsteady aerodynamics and flow control for flapping wing flyers, Progress in Aerospace Sciences, Vol. 39, pp.635-681.*
6. *Huang, S., Cairo, R., Parker, R., Huang G. and Yang, Z. (2013) An experimental vnvestigation on wing optimization for a four- wing flapper, AIAA-2013-0069, 51st AIAA Aerospace Science Meeting, Grapevine, Texas, 2013.*
7. *Huang, X. (1987) Active control of aerofoil flutter. AIAA Journal, Vol. 25, pp.1126-1132.*
8. *Heathcote, S., Wang, Z. and Gursul, I. (2008) Effect of spanwise flexibility on flapping wing propulsion. Journal of Fluids and Structures, Vol. 24, No. 2, pp. 183-199.*
9. *Hsu, C., Evans, J., Vytla, S. and Huang, P. G. (2010) Development of flapping wing Micro Air Vehicles - design, CFD, experiment and actual Flight, AIAA-2010-1018, 48th AIAA Aerospace Science Meeting, Orlando, Florida.*
10. *Hu, H., Gopa-Kumar, A., Abate, G., and Albertani, R. (2010) "An experimental study of flexible membrane wings in flapping flight", Aerospace Science and Technology, Vol.14, No.8, pp575-586.*
11. *Jones, M., and Yamaleev, N. K. (2012) The effect of a gust on the flapping wing performance, 50th AIAA Aerospace Science Meeting, AIAA 2012-1080, Nahshville, Tennessee.*
12. *Koehler, C., Liang, Z., Gaston, Z., Wan, H., and Dong, H. (2012) 3D Reconstruction and Analysis of Wing Deformation in Free-Flying Dragonflies, Journal of Experimental Biology vol.215, pp.3018-3027 .*
13. *Kim, D.K., Kim, H.I., Han, J.H., and Kwon, K.J. (2008) Experimental investigation on the aerodynamic characteristics of a bio- mimetic flapping wing with macro-fiber composites, J. Intell. Mater. Syst. Struct., Vol. 19, pp. 423–431.*

14. *Lin, C., Hwu, C., Young, W. (2006) The thrust and lift of an ornithopter's membrane wings with simple flapping motion.Aerospace Science and Tecchonology, Vol. 10, pp.111-119*
15. *Lighthill, J. (1990) Some Challenging new applications for basic mathematical methods in the mechanics of fluids that were originally pursued with aeronautical aims, Aeronautical Journal, vol. 94, No. 932, pp. 41-52.*
16. *Lu, P-J., and Huang, L-J. (1992) Flutter suppression of thin airfoils using active acoustic excitations, AIAA Journal, Vol. 30, issue 12, pp.2873-2881.*
17. *Massey, K, Flick, A and Jadhav, G. (2009) Force measurements and flow visualization for a flexible flapping wing mechanism.International Journal of Micro Air Vehicles, vol. 1, no. 3, pp. 183-202.*
18. *Mazaheri, K., and Ebrahimi, A. (2010) Experimental investigation of the effect of chordwise flexibility on the aerodynamics of flapping wings in hovering flight, Journal of Fluids and Structures, Vol.26, pp.544-558.*
19. *Mueller, D., Bruck, H.A., Gupta, S.K. (2010) Measurement of Thrust and Lift Forces Associated With Drag of Compliant Flapping Wing for Micro Air Vehicles Using a New Test Stand Design. Experimental Mechanics, Vol. 50, pp.725-735.*

20. *Maxwothy, T. (1979) Experiments on the Weis-Fogh mechanism of lift generation by insects in hovering fight. Part 1.Dynamics of the fling, J Fluid Mech., Vol. 93, pp.47–63.*
21. *Mueller, D., Bruck, H. A., Gupta, S. K. (2010) Measurement of thrust and lift forces associated with drag of compliant flapping wing for Micro Air Vehicles using a new test stand design, Experimental Mechanics, Vol.50, pp.725-735.*
22. *Nissim, E. (1971) Flutter suppression using active control based on the concept of aerodynamic energy, NASA TN-6199.*
23. *Rayner, J. (1979) A vortex theory of animal flight. Part 2. The forward flight of birds, Journal of Fluid Mechanics, Vol. 91, Part 4, pp. 731-763.*
24. *Ricci, R., Montelpare, S., Silvi, E. (2007) Study of acoustic disturbances effect on lamina separation bubble by IR thermography, Experimental Thermal and Fluid Science, 31:349-359.*
25. *Shyy, W., Jenkins, D. A., Smith, R.W. (1997) Study of adaptive shape airfoils at low Reynolds number in oscillatory flow. AIAA Journal, Vol. 35, pp. 1545-1548.*
26. *Shyy, W., Aono, H., Chimarkurthi, S.K., Trizila, P., Kang, C.K., Cesnik, C.E.S., Liu, H. (2010) Recent progress in flapping wing aerodynamics and aeroelasticity. Progress in Aerospace Sciences, Vol. 46, issue7, pp.284-327.*

27. *Spedding, G. R. (1992) The aerodynamics of flight, Mechanics of Animal Locomotion, edited by R. McNeill Alexander, Advanced Comparative Environmental Physiology, Vol. 11, Springer-Verlag, Berlin.*
28. *Suzuki, S., Ishii, K. (2000) Numerical simulation of he acoustic control of separation over 2D airfoils. AIAA paper 2000-1996.*
29. *Thomas, J. M., Fixed and Flapping Wing Aerodynamics for Micro Air Vehicle Applications, Progress in astronuatics and Aeronautics, 2001.*
30. *Treat, A. E. (1955) The response to sound in certain Lepidoptera. Annuals of the Entomological Society of America, 48(4): 272-284.*
31. *Wang, Z. J. (2000) Vortex shedding and frequency selection in flapping flight. J Fluid Mech., Vol. 410, pp.323-341.*
32. *Watman, D. and Furukawa, T. (2008) A visualization system for analysis of Micro Aerial Vehicle scaled flapping wings. Journal of Intelligent and Robotic System, vol. 51, No. 3, pp. 369-381.*
33. *Weis-Fogh, T. (1973) Quick estimates of flight fitness in hovering animals, including novel mechanisms for lift production J. Exp. Biol., vol.59, pp. 169–230*
34. *Wu, P., Peter, I. J., Bret, S. (2010) Flapping Wing structural deformation and thrust correlation study with flexible membrane wings. AIAA Journal, Vol. 48, No. 9, pp.2111-2122.*
35. *Yarusevych, S.m Sullivan, P.E., and Kawall, J.G. (2007) Study of acoustic disturbances effect on laminar separation bubble by IR thermography. Experimental Thermal and Fluid Science, Vol. 31, pp. 349-359.*
36. *Zaman, K.B.M.Q., Mckinzie, D.J. (1991) Control of laminar separation over airfoils by acoustic excitation, AIAA Journal, 29:1075-7083.*
37. *Zarovy, S., Costello, M., Mehta, A., Flynn, A., Gremillion, G., Miller, D., Ranganathan, B., Seen Humbert, J. (2010) Experimental study of gust effects on Micro Air Vehicles, AIAA conference on Atmospheric Flight Mechanics, AIAA-2010-7818, Toronto, Canada.*
38. *Zhu, Q., and Peng, Z. (2009) Mode coupling and flow energy harvesting by a flapping foil. Phys. Fluids., vol.21, 033601.*